

Optical and electrical properties of radio frequency sputtered tin oxide films doped with oxygen vacancies, F, Sb, or Mo

B. Stjerna and E. Olsson

Physics Department, Chalmers University of Technology and University of Gothenburg, S-412 96 Gothenburg, Sweden

C. G. Granqvist

Department of Technology, Uppsala University, P.O. Box 534, S-751 21 Uppsala, Sweden

(Received 22 February 1994; accepted for publication 9 June 1994)

Tin oxide films doped with oxygen vacancies, F, Sb, or Mo were made by reactive rf magnetron sputtering of Sn, Sn-Sb, or Sn-Mo in $\text{Ar}+\text{O}_2(+\text{CF}_4)$ onto glass heated to a temperature up to 530 °C. Electrical dc resistivity, mobility, free-electron density, spectral optical properties, and microstructure were investigated as a function of sputtering parameters. Optimized deposition parameters gave $\text{SnO}_x:(\text{Sb},\text{F})$ films with high luminous transmittance, low luminous absorptance, high infrared reflectance, and dc resistivity down to $9.1\times 10^{-4} \Omega \text{ cm}$. Refractive index n and extinction coefficient k were evaluated from spectrophotometric transmittance. In the luminous range, the films had $1.90 < n < 2.0$ and k of the order of 10^{-2} . Hall-effect measurements showed n -type conduction with electron densities in the 10^{20} – 10^{21} cm^{-3} range. Band-gap broadening from 4.06 to 4.45 eV was observed with increasing electron density. X-ray diffractometry and transmission electron microscopy showed that the structure factor of the films depended on the oxygen content as well as on the specific doping species. A preferred direction of film growth was probably also present. Transmission electron microscopy indicated different grain sizes, between 6 and 30 nm, depending on oxygen content, substrate temperature, and doping species. Optical and electrical properties were compared with results from a quantitative model for wide band-gap semiconductors. The theory is based on heavy n doping by oxygen vacancies or by Sb or/and F and encompasses ionized impurity scattering of the free electrons. It was found that ionized impurity scattering, as well as an additional scattering mechanism tentatively ascribed to grain boundaries, prevailed in the films.

I. INTRODUCTION

This work reports on thin transparent tin oxide films doped with oxygen vacancies, Sb, F, or Mo. The films were made by reactive rf magnetron sputtering onto glass. We discuss the preparation and optimization of the films with respect to low resistivity, high luminous transmittance, and high thermal infrared reflectance. Optical constants and band gaps are given for optimized films. Structural analysis was carried out with several techniques. We also treat the optical properties of doped tin oxide films from basic principles, starting from the contributions to the dielectric function from free carriers, valence electrons, and phonons. A theoretical model embodying energy-dependent ionized impurity scattering was used to calculate the optical transmittance, reflectance, and absorptance and a comparison between theory and experiment is made.

Thin films that combine high luminous transmittance with significant electrical conductivity or infrared reflectance have important applications in energy-efficient architecture,¹ for information displays,² and in many other fields of technology. Certain heavily doped wide band-gap oxide semiconductors—notably those based on Zn, Cd, In, Sn, and alloys of these—have been used for the mentioned applications for many years. Following earlier investigations in our laboratory on $\text{In}_2\text{O}_3:\text{Sn}$ (Ref. 3), $\text{ZnO}:\text{Al}$ (Ref. 4), and SnO_x (Refs. 5 and 6), we have turned in this work to tin oxide doped with either Sb, F, or Mo.

There is extensive literature on conducting doped tin oxide films. Several deposition techniques have been used, e.g., sputtering,^{7–15} spray pyrolysis,^{16–23} chemical-vapor deposition (CVD),^{24–31} and evaporation.^{32–35} Table I contains key data for thin films produced by these various techniques and lists substrate temperature during deposition T_s , sheet resistance R_{sq} , and dc resistivity ρ_{dc} . In most cases, the films were between 0.1 and 1 μm thick. Sputtering seems to be the only technique able to produce films with good electrical conductivity and high visible transmittance for $T_s < 100^\circ\text{C}$ at a high deposition rate. Bearing this in mind, our work was focused on sputtering. It can be seen from Table I that sputtered films generally show higher resistivity than films deposited by other techniques. An apparent exception is for the sputtered $\text{SnO}_x:\text{F}$ films in Ref. 15 which had $\rho_{dc} \approx 0.5 \times 10^{-3} \Omega \text{ cm}$ in the as-deposited state; however, it was reported¹⁵ that such films were unstable and that their electrical properties deteriorated significantly after 6 months of storage.

This paper is organized as follows: Sec. II describes the experimental setup for the preparation of the films. Section III is devoted to process optimization for optical and electrical properties. This part is extensive and treats in detail the important relation between several different deposition parameters and the ensuing film properties. In Sec. IV, an analysis of the optical data is given; results are reported for optical constants and band gaps. Section V covers film characterization with x-ray diffraction and transmission electron

TABLE I. Data for tin-oxide-based films prepared by different techniques. Entries are given for substrate temperature during deposition (τ_s), sheet resistance (R_{sq}), and dc resistivity (ρ_{dc}).

Material	Deposition technique	τ_s (°C)	R_{sq} (Ω)	ρ_{dc} ($\Omega \text{ cm} \times 10^{-3}$)	Ref.
SnO _x	sputtering	Room temp.	90	2.7	5,6
		Room temp.	125	2.5	7
		Room temp.	310	3.7	8
		60	104	2.5	9
		200	665	10	10
		450	610	6.1	11
	spray	400	90	1.48	16
		400	110	2.2	17
		460	8.5	0.45	18
	CVD	450	20	1.0	24
		500	420	4.2	25
		500	40	1.43	26
	evaporation	300	105	5.25	32
		350	...	6.6	33
SnO _x :Sb	sputtering	200	800	8.0	10
		300	140	4.9	12
		350	...	3.0	13
		400	...	2.0	14
		530	41	1.3	this work
		400	15	1.0	19
	spray	530	...	0.9	20
		600	79	0.79	21
		464	11	1.7	27
	CVD	500	55	0.55	25
		450–585	...	0.83	28
		350	10	0.25	32
	evaporation	420	55	3.0	34
		500	58	2.9	35
SnO _x :F	sputtering	450	25	0.5	15
		445	86	2.8	this work
	spray	425	5	0.083	16
		450	20	0.344	22
		680	12	0.4	23
	CVD	400	4.7	0.59	30
		430	34	0.51	31
		478	11	1.7	27
SnO _x :(Sb,F)	sputtering	530	12.5	0.91	this work

microscopy. In Sec. VI, we consider theoretical models of the frequency dependent dielectric function ϵ for doped wide band-gap oxide semiconductors such as tin oxide. Specifically, the free electrons were treated with the approach of Gerlach and Grosse³⁶ as applied to ionized impurity scattering. We compare experimental and theoretical data for transmittance, reflectance, and absorptance. Section VII, finally, summarizes the main results and gives some concluding remarks.

II. PREPARATION OF THIN FILMS

Tin-oxide-based films were made by reactive rf magnetron sputtering. A detailed description of the thin-film deposition system is given in Ref. 37. Evacuation to the low 10^{-6} -Torr range was accomplished by a cryopump connected to the sputter chamber via a gate valve and a louvre baffle throttling valve. The residual gas was monitored by an ionization gauge. The gas pressure during sputtering was measured with a capacitance manometer. Sputter gases were sup-

plied via mass-flow-controlled gas inlets, run through a mixing chamber, and distributed by a perforated toroidal tube surrounding the target. Sputtering was carried out from a 10-cm-diameter planar magnetron cathode powered by a 600-W supply operating at 13.56 MHz and connected via a manual impedance matching network. Substrates were placed on a heater located 55 mm below the target. The true substrate temperature was calibrated by mounting a thermocouple on top of each specific substrate material and running the heater under a normal sputter process gas pressure (4 mTorr of Ar) in the chamber.

The target materials were 99.999%-pure tin, as well as hot-pressed plates of 99.9% tin-antimony with Sb/(Sb+Sn)=2, 4, 6, and 8 at. % and of tin-molybdenum with Mo/(Mo+Sn)=1 and 3 at. %. The sputter gases were 99.9997% Ar, 99.998% O₂, and 99.995% CF₄. Substrates were Corning 7059 glass, standard microscope glass slides, and quartz. Their sizes were, in most cases, $2.5 \times 2.5 \text{ cm}^2$. Before mounting the substrates, they were rinsed in alcohol and blown dry by compressed air.

TABLE II. Deposition conditions for doped tin-oxide-based films.

Parameter	Symbol	Value
rf power	P_{rf}	60 W
Gas pressure	p	4 mTorr
Target-substrate distance	...	55 mm
Substrate temperature	τ_s	23–530 °C
Oxygen gas flow	Γ_{O_2}	5–25 fl. %
Antimony concentration	C_{Sb}	0, 2, 4, 6, 8, at. %
CF ₄ gas flow	Γ_{CF_4}	0–6 fl. %

The aim was to produce reactively sputtered tin-oxide-based films with minimized dc electrical resistivity ρ_{dc} and with maximized luminous transmittance T_{lum} and thermal infrared reflectance. During the optimization of the process, more than 500 samples of tin oxide films doped with oxygen vacancies, Sb, F, or Mo were produced and studied.

Optimization of the sputtering process was done, in most of the experiments, by varying four quantities: (1) the substrate temperature τ_s , (2) the $O_2/[O_2+Ar(+CF_4)]$ gas flow ratio Γ_{O_2} , (3) the antimony content C_{Sb} , and (4) the $CF_4/(O_2+Ar+CF_4)$ gas flow ratio Γ_{CF_4} .

One can consider C_{Sb} and Γ_{CF_4} as “doping parameters.” In some experiments, the molybdenum content C_{Mo} was varied. The rf power delivered to the cathode was kept constant during the fabrication of all films. The film thickness t , determined by surface profilometry using a Tencor Alphastep 200, was kept at 300 ± 70 nm in order to allow easy comparison of measured data. The sputter time lay between 6 and 15 min. Table II lists the parameter values used during sputtering.

III. PROCESS OPTIMIZATION

A. Parameters to optimize

The conductivity of weakly nonstoichiometric tin oxide films is supposed to be due to doubly ionized oxygen vacancies serving as donors.³⁸ Because of their similar ionic radii (1.17 Å for F^- and 1.22 Å for O^{2-}), fluorine (F^-) may substitute for the anion (O^{2-}) in SnO_2 and act as a donor³⁹ in $SnO_x:F$. Furthermore, since the ionic radii of Sn^{4+} and Sb^{5+} are matching²⁰ (Sn^{4+} is 0.71 Å, and Sb^{5+} is 0.65 Å), the cation Sn^{4+} can be substituted by Sb^{5+} , which will act as a donor in $SnO_x:Sb$. Clearly, an optimization of the optical and electrical properties is a demanding task and requires production of films with controlled amounts of oxygen vacancies, fluorine, antimony, and combinations of these dopants.

The object of the optimization process, described in detail in Sec. III B, was to vary the three parameters τ_s , Γ_{CF_4} , and C_{Sb} in order to obtain sputter-deposited tin-oxide-based films with minimum ρ_{dc} in combination with high T_{lum} . The optimization was made in three steps—one step for each of the varied parameters. A complementary study of the effect of Mo doping is given in Sec. III C.

The resistivity of tin oxide films is very sensitive to the oxygen content, and there exists a minimum in the resistivity, denoted ρ_{dc}^* , for a specific oxygen flow ratio Γ^* .^{6,40} During each optimization series, all sputter parameters except Γ_{O_2}

were kept constant in order to find Γ^* . In the first step of the optimization process, we investigated how the resistivity was influenced by the substrate temperature. We produced SnO_x , $SnO_x:F$ ($\Gamma_{CF_4} = 4$ fl. %) and $SnO_x:Sb$ ($C_{Sb} = 8$ at. %) films at different τ_s . The τ_s that gave the lowest ρ_{dc}^* was then used in the following steps.

In the second step, we turned to $SnO_x:F$ and $SnO_x:[Sb(C_{Sb}=4 \text{ at. \%}),F]$ films prepared with varying Γ_{CF_4} . This part of the optimization process gave the final optimized values for the $SnO_x:F$ films. The most favorable Γ_{CF_4} obtained for $SnO_x:[Sb(C_{Sb}=4 \text{ at. \%}),F]$ was then used in the third and last optimization step.

In the third step, C_{Sb} was varied in $SnO_x:Sb$ and $SnO_x:[Sb,F(\Gamma_{CF_4} = 3 \text{ fl. \%})]$ films, and the final optimized values for the antimony-containing films were obtained.

All films were characterized by four parameters: ρ_{dc} , T_{lum} , luminous absorbance A_{lum} , and deposition rate r . The films produced at Γ^* were further characterized by Hall-effect measurements to obtain mobility μ_H and free-electron concentration n_H . These quantities were determined as follows.

Electrical dc resistance was measured on a true square by pressing a probe, connected to an ohm meter, against the film. The probe consisted of two parallel rows of electrically connected Cu pins mounted on springs. The rows were 15 mm long and 15 mm apart. The reading gave R_{sq} , and ρ_{dc} was evaluated from

$$\rho_{dc} = R_{sq} t. \quad (1)$$

The R_{sq} values obtained by this simple procedure were in good agreement with determinations based on the van der Pauw technique.

Spectral normal transmittance $T(\lambda)$ and near-normal reflectance $R(\lambda)$ were measured with double-beam spectrophotometers. A Perkin–Elmer Lambda 9 spectrophotometer was used for wavelengths $0.3 < \lambda < 2.5 \mu\text{m}$, and a Perkin–Elmer 580B spectrophotometer was used for $2.5 < \lambda < 50 \mu\text{m}$. As references for the reflectance measurement, we used a SiO-coated Al mirror at $\lambda < 2.5 \mu\text{m}$ and a Au mirror at $\lambda > 2.5 \mu\text{m}$. Spectral absorbance was then evaluated from

$$A(\lambda) = 1 - T(\lambda) - R(\lambda). \quad (2)$$

Quantitative assessments of the optical properties were made by averaging the spectral data over the standard luminous efficiency for photopic vision $V(\lambda)$.⁴¹ The luminous transmittance was computed from

$$T_{lum} = \int d\lambda T(\lambda) V(\lambda) / \int d\lambda V(\lambda), \quad (3)$$

and analogous expressions were used for R_{lum} and A_{lum} .

The deposition rate, which is an important parameter for practical thin-film fabrication, was calculated as the ratio between film thickness and sputtering time.

For Hall-effect measurements, coated glass substrates were cut into $4 \times 4 \text{ mm}^2$ squares, and the van der Pauw four-point method was used to obtain μ_H and n_H .

The data for the optimized tin oxide films, presented below, clearly pertain to a specific sputter configuration and

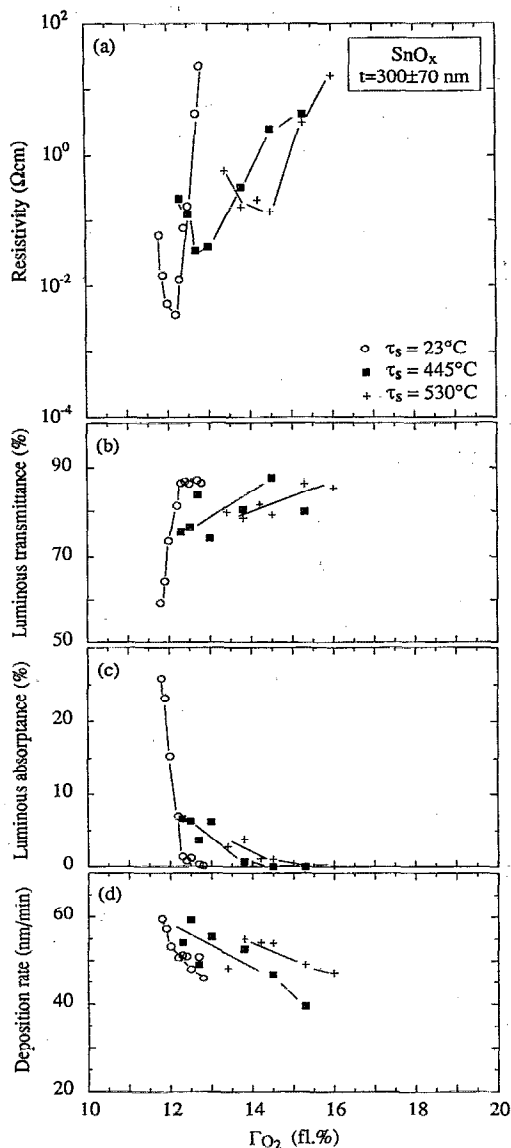


FIG. 1. Resistivity, luminous transmittance, luminous absorbance, and deposition rate for tin oxide films sputtered at the relative oxygen content Γ_{O_2} onto substrates at the temperature τ_s . Symbols denote measured results, and lines, connecting adjacent data points, were drawn for convenience.

deposition system. However, we believe that the various parameter dependencies are of general validity, although the numerical values may well be somewhat different for other target-substrate configurations, sputter gas pressures, etc.

B. Doping with oxygen vacancies, F, and Sb

1. Optimization of substrate temperature

Figure 1 reports resistivity, luminous transmittance, luminous absorbance, and deposition rate versus Γ_{O_2} for SnO_x films. Part (a) shows that there is a general increase of the resistivity for SnO_x films with increasing τ_s , and that the minimum resistivity occurs for a certain well defined value for the gas flow ratio. It is also seen that ρ_{dc}^* occurs at higher Γ^* for higher τ_s . A substrate kept at room temperature yields

a ρ_{dc}^* of $\sim 3.8 \times 10^{-3} \Omega \text{ cm}$. It is possible to further decrease the resistivity by decreasing the rf power during the deposition, as found in earlier work of ours.^{5,6} T_{lum} in Fig. 1(b) reaches 80%–85% for the films prepared with high Γ_{O_2} at all τ_s , whereas the T_{lum} is much lower at low Γ_{O_2} , especially for films made with substrates at room temperature. When a small amount of Γ_{O_2} was used during the deposition, the films were visibly yellow, probably due to SnO -like inclusions in the SnO_2 matrix.⁴² Consequently A_{lum} in Fig. 1(c) is high for films with low Γ_{O_2} . In Fig. 1(d) it can be seen that the deposition rate is not strongly dependent on τ_s . It is about 50 nm/min for the films showing a minimum in resistivity.

Figures 2 and 3 give the same information as in Fig. 1, but for films containing Sb and F. The films in Fig. 2 were doped with 8 at. % Sb. In part (a), the resistivity is shown as a function of Γ_{O_2} for three different values of τ_s (235, 460, and 530 °C). Similar measurements were also made for the substrate temperatures 23, 295, and 370 °C. The resistivity minima for the films become deeper with increasing substrate temperature. At $\tau_s = 530$ °C, the resistivity is virtually independent of the oxygen flow rate as long as $\Gamma_{O_2} > \Gamma^*$; its minimum lies at $\rho_{dc}^* \sim 1.3 \times 10^{-3} \Omega \text{ cm}$. In Fig. 2(b) it can be seen that T_{lum} shows a minimum at Γ^* only for films made at high τ_s (460 and 530 °C). Such behavior was observed also for films with $C_{Sb} = 6$ at. %. Figure 2(c) shows a high value of A_{lum} , roughly 20%, except at $\tau_s = 530$ °C and $\Gamma_{O_2} < \Gamma^*$. The deposition rate reported in Fig. 2(d) is about the same as that for the SnO_x films in Fig. 1(d), i.e., about 50 nm/min for films at Γ^* . The rate decreases with increasing Γ_{O_2} .

Figure 3 is devoted to tin-oxide-based films doped with 4 fl. % CF_4 . In part (a) it can be seen that the lowest resistivity is obtained at $\tau_s = 445$ °C, which gives $\rho_{dc}^* \sim 2.8 \times 10^{-3} \Omega \text{ cm}$. It is evident that the resistivity shows only a weak dependency on the oxygen flow ratio for $7 < \Gamma_{O_2} < 13$ fl. % at all three values of τ_s . The luminous transmittance, as shown in Fig. 3(b), exceeds 80% for the SnO_x :F films at Γ^* , independently of τ_s . The luminous absorbance, reported in Fig. 3(c), shows an overall decrease with increasing τ_s and an A_{lum} as low as about 2% for the films with lowest resistivity. The deposition rate in Fig. 3(d) shows a slight decrease with increasing τ_s . The rate is about 40 nm/min for the films with lowest resistivity, which is significantly lower than the rate for the SnO_x and SnO_x :Sb (8 at. %) films reported on in Figs. 1(d) and 2(d).

Figure 4 summarizes and extends the results of Figs. 1–3. Each data point in Fig. 4 pertains to a minimum in resistivity from one of the sequences of results in Figs. 1–3. Some results from sequences not presented before are included in Fig. 4 as well. Besides the earlier shown quantities, results are reported for the free-electron concentration and the electrical mobility, as obtained from Hall-effect measurements. It is seen that the resistivity of the films with $C_{Sb} = 8$ at. % decreases with increasing τ_s . At $\tau_s = 530$ °C, we obtained $\rho_{dc}^* \approx 1.3 \times 10^{-3} \Omega \text{ cm}$. We were not able to produce films at higher τ_s due to limitations in the substrate heater.

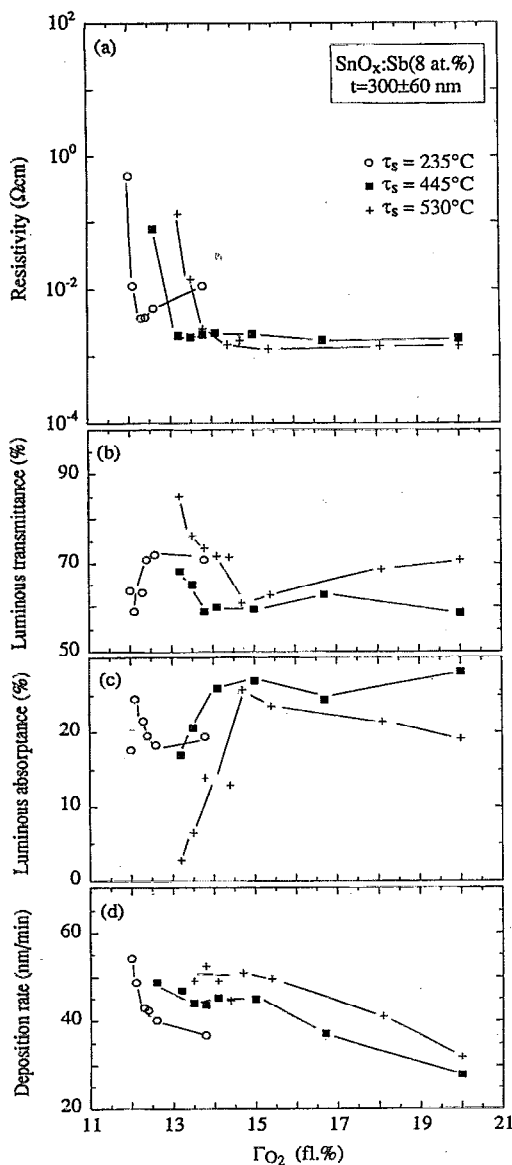


FIG. 2. Resistivity, luminous transmittance, luminous absorbance, and deposition rate for antimony doped tin oxide films sputtered at the relative oxygen content Γ_{O_2} onto substrates at the temperatures τ_s . Symbols denote measured results, and lines, connecting adjacent data points, were drawn for convenience.

The films with $C_{Sb}=8$ at. % appeared dark blue in color, probably because of small amounts of occluded Sb_2O_3 and Sb_2O_5 .⁴³ Films produced with heated substrates have a T_{lum} as low as $\sim 60\%$ and $A_{lum} > 20\%$.

For films doped with $\Gamma_{CF_4} = 4$ fl. %, Fig. 4 shows a weak minimum in resistivity, and $\rho_{dc}^* \approx 2.8 \times 10^{-3} \Omega \text{ cm}$ was observed for $\tau_s = 445^\circ \text{C}$. When τ_s was increased to 530°C , ρ_{dc}^* became larger and some of the F-doped films looked somewhat hazy. The SnO_x films differ from the Sb- and F-doped ones in that ρ_{dc}^* went up when τ_s was enhanced. The lowest resistivity in the case of SnO_x was obtained for films produced at room temperature, which gave $\rho_{dc}^* \approx 3.8 \times 10^{-3} \Omega \text{ cm}$. In Sec. V B below it will be shown that the grain size in SnO_x films increases with increasing τ_s , which

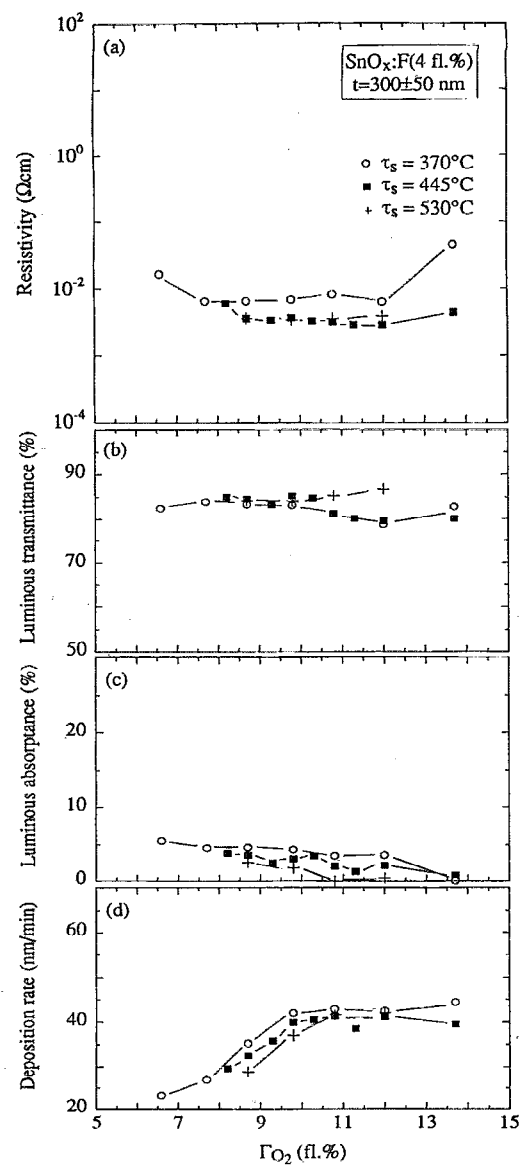
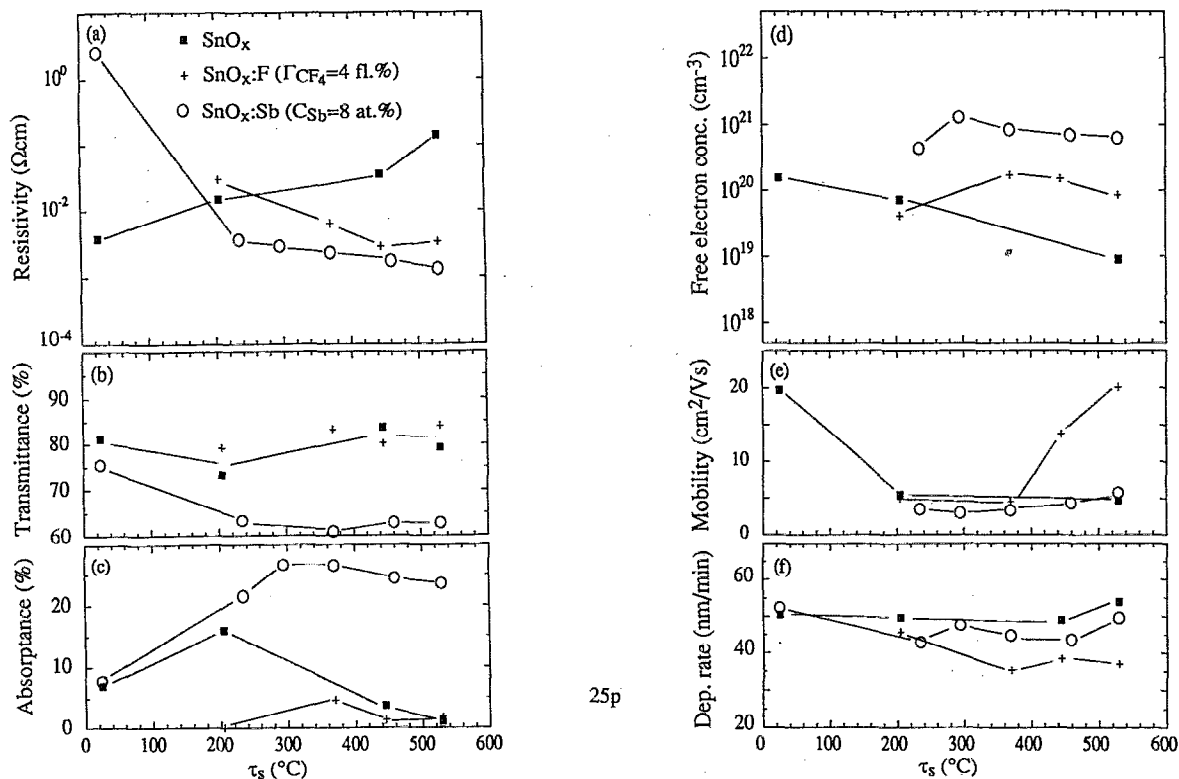


FIG. 3. Resistivity, luminous transmittance, luminous absorbance, and deposition rate for fluorine-doped tin oxide films sputtered at the relative oxygen content Γ_{O_2} onto substrates at the temperatures τ_s . Symbols denote measured results, and lines, connecting adjacent data points, were drawn for convenience.

normally would lead to a decrease in ρ_{dc}^* . However, in Figs. 4(d) and 4(e) it can be seen that the increase of ρ_{dc}^* is related to a decrease of both n_H and μ_H with increasing τ_s . The decrease of n_H indicates that it is not possible to obtain as many oxygen vacancies in SnO_x films produced at high temperatures as it is at room temperature.

Films doped with oxygen vacancies or $\Gamma_{CF_4} = 4$ fl. % are more transparent and less absorbing than films doped with $C_{Sb}=8$ at. %. In Figs. 4(b) and 4(c) it is seen that the F-doped and undoped films have a T_{lum} of $\sim 80\% - 85\%$ and an A_{lum} of $\sim 0\% - 5\%$ for high substrate temperatures.

Figure 4(d) shows that the free-electron concentration at high τ_s is $> 6 \times 10^{20} \text{ cm}^{-3}$ for films with $C_{Sb}=8$ at. %. It is also found that n_H is $\sim 1 \times 10^{20} \text{ cm}^{-3}$ for films with Γ_{CF_4}



25p

FIG. 4. Resistivity, luminous transmittance, luminous absorbance, free-electron concentration, Hall mobility, and deposition rate for tin-oxide-based films sputtered at the optimized relative oxygen content Γ^* onto substrates at the temperature τ_s . Different symbols pertain to variously doped films, as indicated in the figure. Symbols denote measured results, and lines, connecting adjacent data points, were drawn for convenience.

$= 4$ fl. %, and that n_H is about one order of magnitude lower for undoped films ($\sim 1 \times 10^{19} \text{ cm}^{-3}$). The mobility, shown in Fig. 4(e), is low for all samples; it is $\sim 5 \text{ cm}^2/\text{V s}$ for undoped and Sb-doped films at $\tau_s > 200^\circ\text{C}$, and it increases slightly with τ_s for F-doped films and reaches $20 \text{ cm}^2/\text{V s}$ at 530°C .

A comparison with published results on μ_H for sputter-deposited films shows good agreement for undoped SnO_x (Refs. 7, 8, and 11) and for $\text{SnO}_x:\text{Sb}$.^{12,14} For F-doped films, we are not aware of earlier results on μ_H . The highest mobility reported for SnO_2 crystals at room temperature is $260 \text{ cm}^2/\text{V s}$.^{44,45}

Figure 4(f) reports that the deposition rate varies both with substrate temperature and with type of doping. At low τ_s , the rate is about 50 nm/min . For the case of F doping, the rate drops when τ_s is increased and is $< 40 \text{ nm/min}$ for $\tau_s > 370^\circ\text{C}$. The influence of Γ_{CF_4} will be discussed in more detail below. Films doped with 8 at. % Sb seem to have a slightly lower deposition rate than undoped films, at least at high τ_s .

It is of interest to compare the optimized substrate temperatures for the Sb- and F-doped tin oxide films—i.e., 530 and 445°C , respectively—with results reported for other deposition techniques. Low resistivity, below $10^{-3} \Omega \text{ cm}$, was obtained with CVD^{25,31} and spray^{21,22} techniques at substrate temperatures in the 400 – 600°C range, which clearly is in line with our data.

In the optimization of Γ_{CF_4} and C_{Sb} , reported below, we used $\tau_s = 445^\circ\text{C}$ and $\tau_s = 530^\circ\text{C}$, respectively.

2. Optimization of CF_4 flow

Figure 5 shows ρ_{dc} , T_{lum} , A_{lum} , and r for $\text{SnO}_x:\text{F}$ films doped through sputtering in plasmas containing 1.5, 2.5, and 4.0 fl. % CF_4 . The results for the $\text{SnO}_x:\text{F}$ (4 fl. %) films are the same as those in Fig. 3 at $\tau_s = 445^\circ\text{C}$. In Fig. 5(a) it can be seen that ρ_{dc} is weakly dependent on Γ_{CF_4} , and that the Γ_{O_2} range in which a low resistivity is obtained is broadened for increased Γ_{CF_4} . Figures 5(b) and 5(c) show that T_{lum} is about 80% and A_{lum} is about 2% – 3% for the $\text{SnO}_x:\text{F}$ films prepared at Γ^* . Figure 5(d) reports deposition rates for variously F-doped SnO_x films. It is clearly seen that r is decreased from 55 to 40 nm/min when Γ_{CF_4} is increased from 1.5 to 4.0 fl. %. For $\Gamma_{\text{CF}_4} = 1.5$ fl. %, the deposition rate is higher than that for the SnO_x and $\text{SnO}_x:\text{Sb}$ films.

Figure 6 gives results for films doped with 4 at. % Sb and produced with either 0.85, 1.70, or 3.00 fl. % CF_4 in the sputter plasma. In part (a), showing the resistivity, it can be seen that an increase of Γ_{CF_4} leads to a broadening of the Γ_{O_2} range in which a low resistivity is obtained and a shift of the resistivity minimum towards smaller Γ_{O_2} occurs. There is a concomitant lowering of the deposition rate, shown in Fig. 6(d), and hence it is not clear whether a larger amount of F is

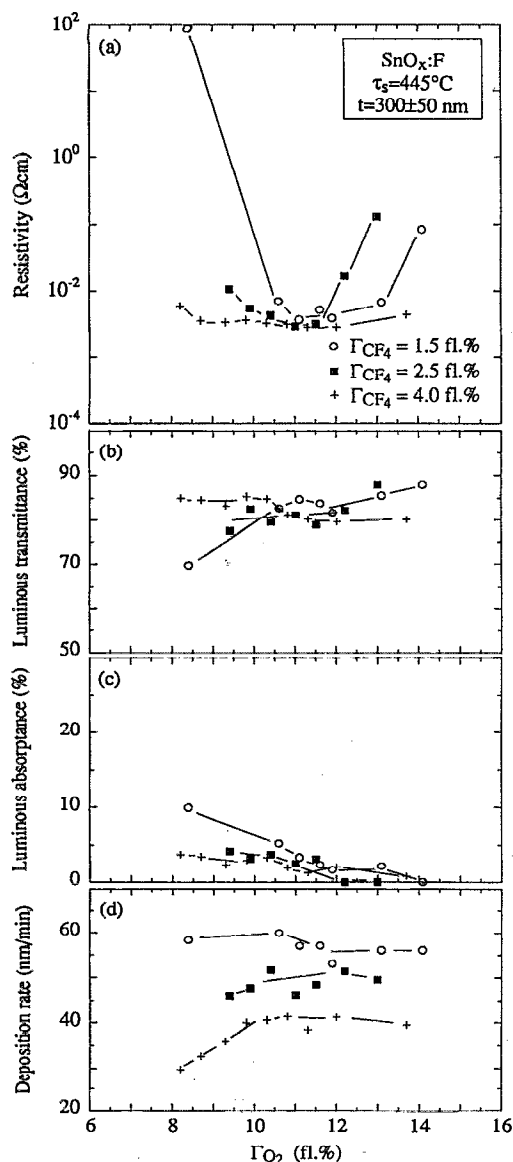


FIG. 5. Resistivity, luminous transmittance, luminous absorbance, and deposition rate for fluorine-doped tin oxide films sputtered at the relative oxygen content Γ_{O_2} and the relative carbon tetrafluoride content Γ_{CF_4} onto substrates heated to 445 °C. Symbols denote measured results, and lines, connecting adjacent data points, were drawn for convenience.

incorporated in the film at high Γ_{CF_4} . In Figs. 6(b) and 6(c) it can be seen that T_{lum} is about 80% and A_{lum} is about 5% for films made at Γ^* , independently of Γ_{CF_4} .

Figure 7 summarizes the results on the optimization of Γ_{CF_4} , reported in detail in Figs. 5 and 6, for the same measured properties as in Fig. 4. Clearly there is no strong dependency on Γ_{CF_4} . It is found that $\Gamma_{CF_4} \sim 3$ fl. % gives a lowest resistivity of $\sim 2\text{--}3 \times 10^{-3} \Omega \text{ cm}$ for purely F-doped tin oxide. We are only aware of one earlier publication for sputtered $\text{SnO}_x\text{:F}$, wherein Geoffroy *et al.*¹⁵ reported $\rho_{dc} \approx 0.5 \times 10^{-3} \Omega \text{ cm}$. They also found that the resistivity of the films increased significantly during 6 months of storage in air. It is worth noting that our results for the resistivity of

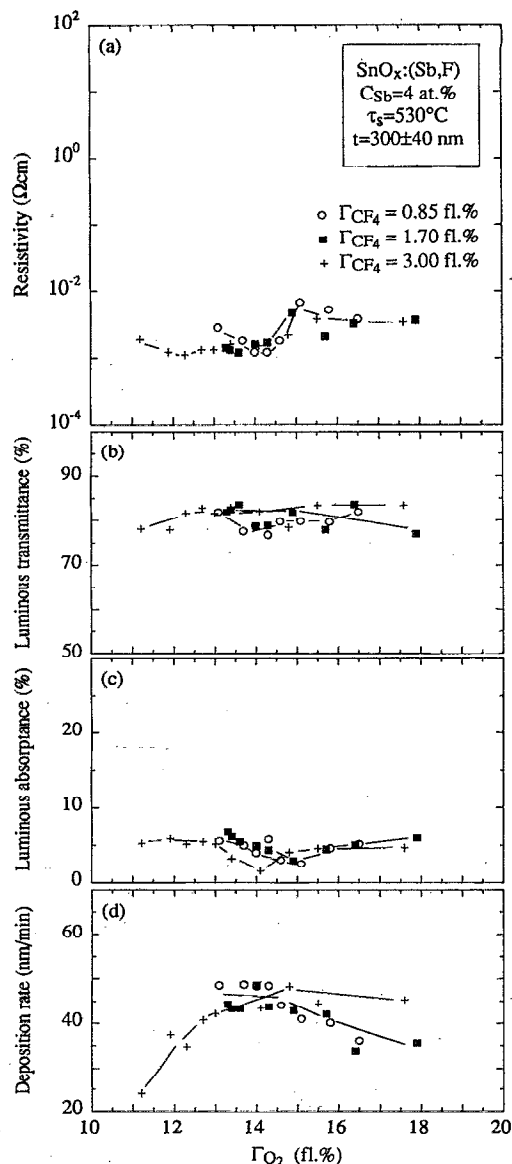


FIG. 6. Resistivity, luminous transmittance, luminous absorbance, and deposition rate for fluorine plus antimony doped tin oxide films sputtered from targets with 4 at. % antimony at the relative oxygen content Γ_{O_2} and the relative carbon tetrafluoride content Γ_{CF_4} onto substrates heated to 530 °C. Symbols denote measured results, and lines, connecting adjacent data points, were drawn for convenience.

sputtered films are 4–10 times higher than those reported for $\text{SnO}_x\text{:F}$ films made by CVD³¹ and spray techniques.²² A difference in grain size, depending on the deposition method, is a possible explanation of the difference in resistivity. We will return to this issue in Sec. V B.

Figure 7(a) indicates that a combination of Sb doping and F doping gives a lower resistivity than for the purely F-doped tin oxide by a factor of 2–3; for $C_{Sb}=4$ at. % and $\Gamma_{CF_4} = 3$ fl. %, one finds $\rho_{dc}^* \approx 1.1 \times 10^{-3} \Omega \text{ cm}$. We used $\Gamma_{CF_4} = 3$ fl. % in combination with varied C_{Sb} during step 3 of the optimization process in order to minimize the resistivity of the $\text{SnO}_x\text{:}(Sb,F)$ films. The obtained results will be reported in Sec. III B 3.

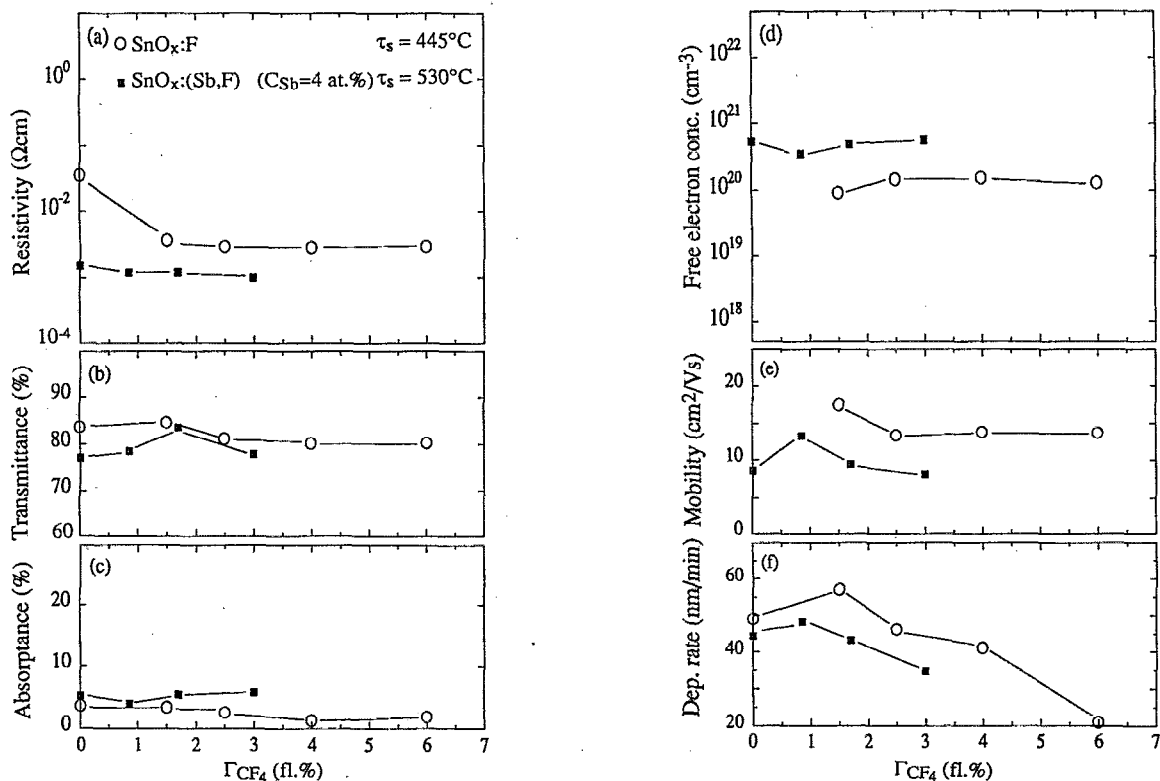


FIG. 7. Resistivity, luminous transmittance, luminous absorbance, free-electron concentration, Hall mobility, and deposition rate for tin-oxide-based films sputtered at the optimized relative oxygen content Γ^* and the relative carbon tetrafluoride content Γ_{CF_4} . Different symbols pertain to films doped with only fluorine and with fluorine plus antimony. The substrate temperature is τ_s . Symbols denote measured results, and lines, connecting adjacent data points, were drawn for convenience.

Figures 7(b) and 7(c) show a T_{lum} as high as $\sim 80\%$ and an A_{lum} as low as $\sim 1\%$ – 5% for films doped with CF_4 . When 4 at. % Sb was added, T_{lum} decreased by a few percent, and A_{lum} showed a corresponding increase. T_{lum} and A_{lum} were almost constant when Γ_{CF_4} was increased, and only a small tendency towards a lower T_{lum} and a higher A_{lum} was observed.

In Figs. 7(d) and 7(e) it is seen that n_H is higher and μ_H is lower for the films doped with both Sb and F than that for the purely F-doped ones. Doping of tin oxide through deposition with $\Gamma_{CF_4} = 1.5$ fl. % enlarged n_H by an order of magnitude, from 1.5×10^{19} to $1.5 \times 10^{20} \text{ cm}^{-3}$. However, n_H was not increased when Γ_{CF_4} was further increased. A similar result was obtained for the films with $C_{Sb} = 4$ at. %, which showed $n_H \approx 5 \times 10^{20} \text{ cm}^{-3}$ for all values of Γ_{CF_4} . As mentioned above in connection with Fig. 4, F-doped films had higher mobilities than undoped and Sb-doped ones. Similarly, when films with $C_{Sb} = 4$ at. % were deposited in the presence of 0.8 fl. % Γ_{CF_4} , an increase in the mobility was observed, as apparent from Fig. 7(e). A further increase of Γ_{CF_4} led to a decrease in μ_H .

According to Fig. 7(f), the deposition rate has a maximum at a moderately low Γ_{CF_4} and then decreases when Γ_{CF_4} is further increased. This result may seem unexpected, since in many cases the addition of CF_4 causes an increase in the deposition rate as a consequence of “chemical

sputtering.”^{46,47} Earlier we have shown this to be true for tin oxide films sputtered onto substrates at room temperature.^{48,49} The present results, displayed in Fig. 4(f), show that when CF_4 is added, the deposition rate decreases with increasing substrate temperature, so that there is no discrepancy with our earlier findings.

3. Optimization of antimony content

Figure 8 shows ρ_{dc}^* , T_{lum} , A_{lum} , and r vs Γ_{O_2} for $SnO_x:Sb$ (2, 4, and 8 at. %) films deposited at $\tau_s = 530^\circ\text{C}$. The results for the $SnO_x:Sb$ (8 at. %) films are the same as those in Fig. 2 at the pertinent τ_s . Part (a) shows that ρ_{dc}^* decreases with increasing C_{Sb} . It can also be seen that when C_{Sb} is increased, the resistivity gets less dependent on the oxygen flow rate for $\Gamma_{O_2} > \Gamma^*$. Figures 8(b) and 8(c) show that T_{lum} decreases and A_{lum} increases with increasing C_{Sb} . The $SnO_x:Sb$ (2 at. %) films combine a resistivity as low as $1.9 \times 10^{-3} \Omega \text{ cm}$, a T_{lum} as high as 80.2%, and an A_{lum} as low as 1.3%. The deposition rate, reported in Fig. 8(d), is about 50 nm/min for the films with the lowest resistivity; it decreases with increasing oxygen flow rate.

Figure 9 contains results for films doped by deposition with 3 fl. % CF_4 and either 2, 4, or 8 at. % Sb. There is a weak minimum in the resistivity for films doped through a combination of 3 fl. % CF_4 and 4 at. % Sb, and ρ_{dc}^* reaches $1.1 \times 10^{-3} \Omega \text{ cm}$. Figure 9(b) shows that a T_{lum} of over 80%,

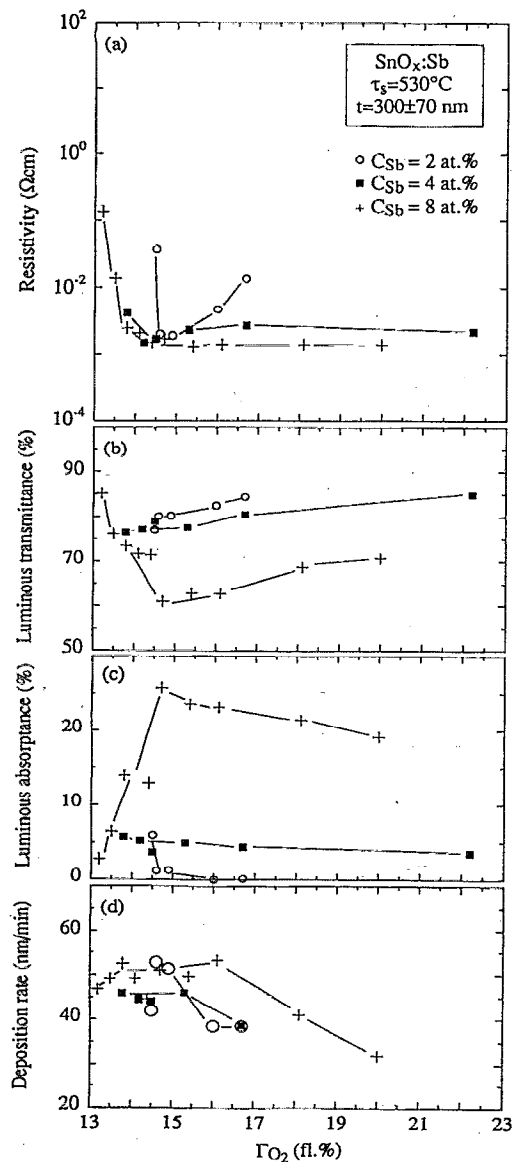


FIG. 8. Resistivity, luminous transmittance, luminous absorptance, and deposition rate for antimony doped tin oxide films sputtered from targets with the antimony content C_{Sb} at the relative oxygen content Γ_{O_2} onto substrates heated to 530 °C. Symbols denote measured results, and lines, connecting adjacent data points, were drawn for convenience.

for films with a low resistivity, is obtained as long as $C_{\text{Sb}} \leq 4$ at. %. However, if $C_{\text{Sb}} = 8$ at. %, T_{lum} falls to about 70%. Consequently, A_{lum} in Fig. 9(c) is high for the films doped with 8 at. % Sb, whereas A_{lum} is about 5% for the films at ρ_{dc}^* and C_{Sb} equal to 2 or 4 at. %. The deposition rates for the films with ρ_{dc}^* are about 40–45 nm/min, irrespective of C_{Sb} . It can also be seen in Fig. 9(d) that the deposition rate decreases drastically when Γ_{O_2} is reduced while Γ_{CF_4} is kept at 3% of the total gas flow.

Figure 10 summarizes the optimization of C_{Sb} , reported in Figs. 8 and 9, for the same measured properties as in Figs. 4 and 7. Part (a) shows that ρ_{dc}^* decreases with increasing C_{Sb} for the purely Sb-doped films. At $C_{\text{Sb}} = 8$ at. %, a resistivity of $1.3 \times 10^{-3} \Omega \text{ cm}$ was obtained. A combination of Sb

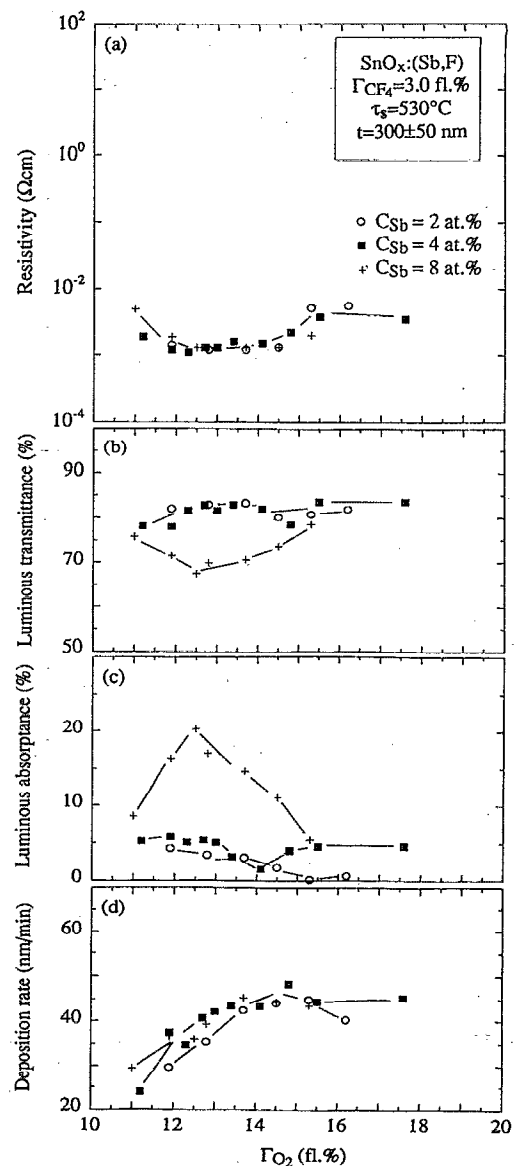


FIG. 9. Resistivity, luminous transmittance, luminous absorptance, and deposition rate for fluorine plus antimony doped tin oxide films sputtered from targets with the antimony content C_{Sb} at the relative oxygen content Γ_{O_2} and a relative carbon tetrafluoride content of 3 fl. % onto substrates heated to 530 °C. Symbols denote measured results, and lines, connecting adjacent data points, were drawn for convenience.

doping with $\Gamma_{\text{CF}_4} = 3$ fl. % yielded a lower ρ_{dc}^* for a C_{Sb} of 2–6 at. % than that for the purely Sb-doped films. The lowest resistivity ($\rho_{\text{dc}}^* \approx 1.1 \times 10^{-3} \Omega \text{ cm}$) was reached for $C_{\text{Sb}} = 4$ at. %. We also made a few films with varying thicknesses. When the thickness was increased from ~ 300 to 725 nm for films doped with $C_{\text{Sb}} = 2$ at. % and $\Gamma_{\text{CF}_4} = 3$ fl. %, the resistivity decreased marginally from 1.2 to $0.9 \times 10^{-3} \Omega \text{ cm}$.

We may compare the present results for the resistivity of Sb-doped tin oxide films with earlier reported data. Suzuki and Mizuhashi¹⁴ found $\rho_{\text{dc}}^* \approx 2.0 \times 10^{-3} \Omega \text{ cm}$ for sputtered Sb-doped tin oxide films, which is somewhat higher than for our best films. We are not aware of any earlier results for sputtered tin oxide films doped with both Sb and F. Results

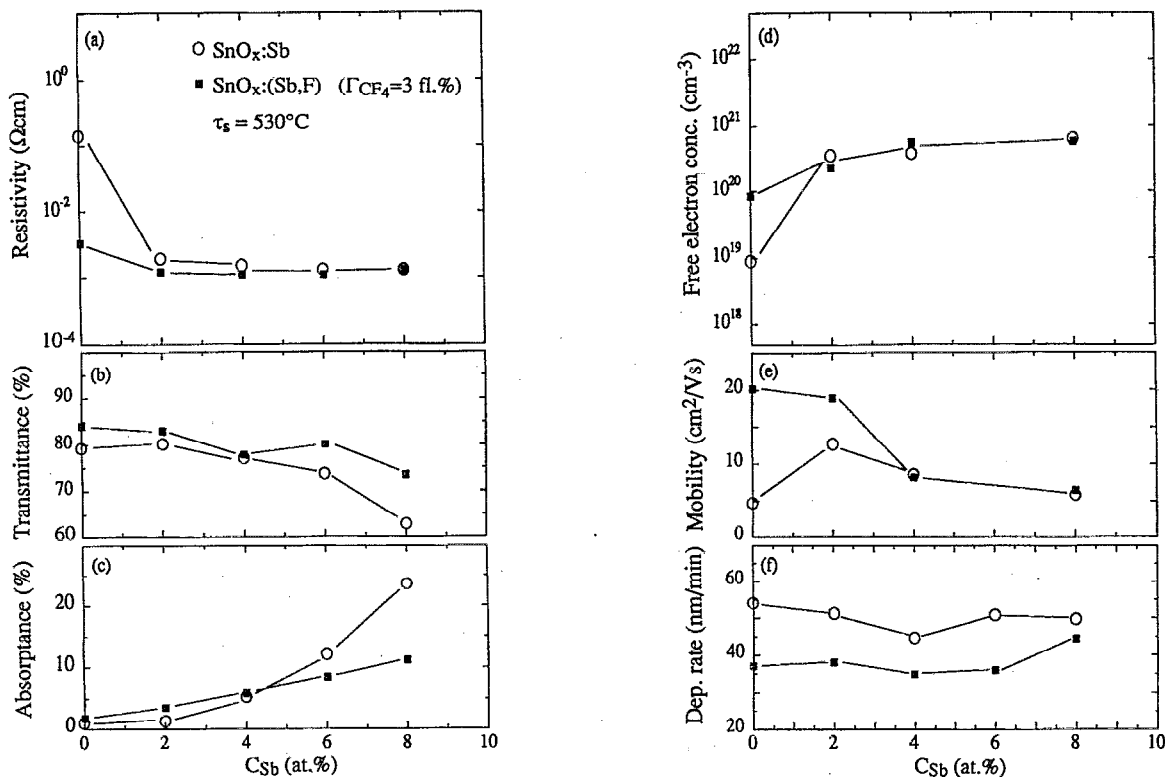


FIG. 10. Resistivity, luminous transmittance, luminous absorbance, free-electron concentration, Hall mobility, and deposition rate for tin-oxide-based films sputtered from targets with the antimony content C_{Sb} at the optimized relative oxygen content Γ^* and the relative carbon tetrafluoride content Γ_{CF_4} . Different symbols pertain to films doped with only antimony and with fluorine plus antimony. The substrate temperature is τ_s . Symbols denote measured results, and lines, connecting adjacent data points, were drawn for convenience.

for spray deposited Sb-doped films,^{19–21} however, show resistivities of about $1 \times 10^{-3} \Omega \text{ cm}$. Shanti *et al.*⁵⁰ reported results for films doped with a combination of Sb and F and deposited by spray pyrolysis. They obtained $\rho_{\text{dc}} \approx 0.8 \times 10^{-3} \Omega \text{ cm}$, which was somewhat higher than for their purely F-doped films. Sb-doped films prepared by CVD^{25,26} and evaporation³² have been reported to show resistivities from about 0.3 to $0.8 \times 10^{-3} \Omega \text{ cm}$. As mentioned above, one possible explanation of the difference in resistivity can be a variation in grain size depending on the deposition technique. We will discuss this further in Sec. V B.

Figure 10(b) shows that an incorporation of fluorine increases T_{lum} , especially at high C_{Sb} . A T_{lum} of about 80%–85% is found for films doped with 2–6 at. % Sb and 3 fl. % CF_4 . About the same T_{lum} was observed earlier for SnO_x and $\text{SnO}_x \cdot \text{F}$ films. The luminous absorbance of Sb-doped films was reduced when F was added to the films with a C_{Sb} of 6 or 8 at. %. From Fig. 10(c) it is apparent that A_{lum} increases with increasing C_{Sb} both for $\text{SnO}_x \cdot \text{Sb}$ and $\text{SnO}_x \cdot (\text{Sb}, \text{F})$. For the films with C_{Sb} being 2 and 4 at. %, an A_{lum} of 2%–6% was obtained. The presence of F is seen to enhance A_{lum} for these low magnitudes of C_{Sb} .

From Figs. 10(d) and 10(e) it is apparent that C_{Sb} governs the values of n_H and μ_H , except at low C_{Sb} where deposition in the presence of CF_4 leads to an increase in the mobility. In the Sb-doped films, an increase of the electron density with increasing C_{Sb} was obtained from

$n_H \sim 3.5 \times 10^{20} \text{ cm}^{-3}$ at $C_{\text{Sb}} = 2$ at. % to $n_H \approx 6.3 \times 10^{20} \text{ cm}^{-3}$ at $C_{\text{Sb}} = 8$ at. %. Deposition with $\Gamma_{\text{CF}_4} = 3$ fl. % did not produce any further enhancement of the electron concentration.

Figure 10(f) shows that r was decreased by about 10 nm/min when 3 fl. % of CF_4 was added to the sputter plasma. Specifically, the rate went from ~ 50 to ~ 40 nm/min. This drop of r , resulting from fluorine doping, was illustrated and discussed above in relation to Figs. 4 and 7.

C. Doping with Mo

Casey and Stephenson⁵¹ recently reported results suggesting that the doping of tin oxide with small quantities of Mo would lead to a material with low resistivity. In an attempt to verify these findings, we prepared films by sputtering from tin targets with 1 or 3 at. % Mo onto substrates at 23 and 530 °C. Figure 11 shows data for films prepared at $\tau_s = 23$ °C, and for comparison, results are given also for SnO_x films doped only with oxygen vacancies. The results for $C_{\text{Mo}} = 1$ at. % are almost identical to those for SnO_x whereas a higher resistivity, a lower luminous transmittance, and a lower deposition rate are obtained with $C_{\text{Mo}} = 3$ at. %. Figure 11(a) shows that for films doped with 3 at. % Mo, the resistivity minimum is shifted towards lower Γ_{O_2} . When $\text{SnO}_x \cdot \text{Mo}$ films were deposited onto substrates at $\tau_s = 530$ °C, their resistivities always were higher than $10^2 \Omega \text{ cm}$.

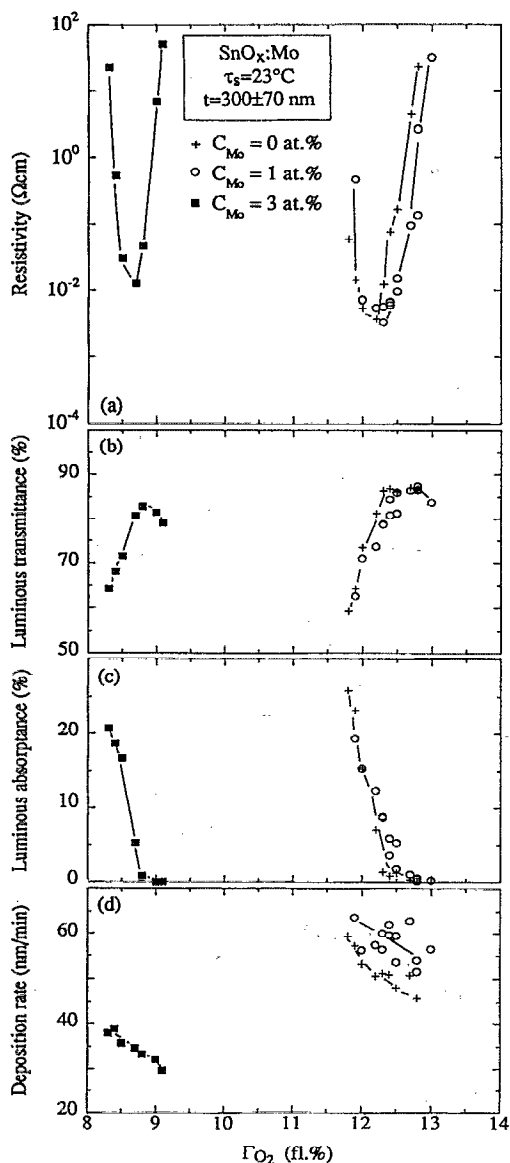


FIG. 11. Resistivity, luminous transmittance, luminous absorptance, and deposition rate for molybdenum-doped tin oxide films sputtered from targets with the molybdenum content C_{Mo} at the relative oxygen content Γ_{O_2} . The substrates were kept at 23 °C. Symbols denote measured results, and lines, connecting adjacent data points, were drawn for convenience.

The conclusion from our study is that the doping of tin oxide with Mo does not decrease the resistivity. We are not able to explain the low resistivities found in the work by Casey and Stephenson,⁵¹ but we wish to draw attention to the critical influence of oxygen vacancies in tin-oxide-based films. Thus the two different deposition situations, for undoped and Mo-doped films in the earlier work, may have given significantly different amounts of oxygen vacancies and consequently, vastly different electrical properties. The fact that the films studied by Casey and Stephenson showed increasing resistivity when stored in air for some weeks also indicates that there existed a large density of oxygen vacancies in the as-deposited films, and that oxidation then might have proceeded as a result of oxygen diffusion from the am-

bience. This oxidation would change the resistivity rapidly, since the films studied by Casey and Stephenson had thicknesses as small as between 3 and 85 nm.

IV. ANALYSIS OF OPTICAL PROPERTIES FOR OPTIMIZED FILMS

A. Spectral transmittance, reflectance, and absorptance

The process optimization, discussed above, used wavelength-integrated optical quantities. However, a more detailed discussion of the optical properties requires spectral data, as we discuss here. Figure 12 shows $T(\lambda)$ and $A(\lambda)$ at $0.3 < \lambda < 2.5 \mu\text{m}$ and $R(\lambda)$ at $0.3 < \lambda < 50 \mu\text{m}$ for five different optimized films: one SnO_x film doped only with oxygen vacancies, one F-doped film, one Sb-doped film, and two films doped with both Sb and F. Detailed information about these films is given in Table III.

The films showed a T_{lum} as high as $\sim 80\%$ and an A_{lum} as low as $< 10\%$, except the $\text{SnO}_x:\text{Sb}$ film in Fig. 12(c), which had $T_{lum} = 62.8\%$ and $A_{lum} = 23.5\%$. The low T_{lum} and high A_{lum} of the $\text{SnO}_x:\text{Sb}$ film are associated with the heavy doping with 8 at. % Sb, and the film was visibly dark blue. The onset of high reflectance occurred at a short wavelength for the $\text{SnO}_x:\text{Sb}$ film and is due to the free-electron concentration being as high as $0.63 \times 10^{21} \text{ cm}^{-3}$. This is about three times higher than that for the other film materials.

A high infrared reflectance requires a low resistance/square, which calls for films with low resistivity and a large thickness [cf. Eq. (1)]. Table III lists resistance/square for the films whose reflectance is illustrated in Fig. 12. Comparing the infrared reflectance with the R_{sq} values, it is apparent that the infrared reflectance indeed increases with decreasing R_{sq} .

The oscillations of T and R in the visible part of the spectrum are caused by optical interference. In the infrared region, several phonon peaks can be seen. According to the literature,^{45,52} phonon peaks are expected at 16.3, 21.0, 34.2, and 41.1 μm in tin oxide, which is in good agreement with our results as well as with data reported elsewhere.^{53,54}

The best combination of high luminous transmittance, low luminous absorptance, and high infrared reflectance was obtained with joint Sb and F doping. Figures 12(d) and 12(e) show results for films sputtered with the same parameters during different times, so that different thicknesses were reached. The film reported on in Fig. 12(e) is thick ($t = 725 \text{ nm}$) and has $\rho_{dc}^* \approx 9.1 \times 10^{-4} \Omega \text{ cm}$, which gives $R_{sq} \approx 12.5 \Omega$. Despite the large thickness, the film had an A_{lum} as low as 7.5%, a T_{lum} as high as 79.7%, and an infrared reflectance in the 70%–90% range. At $t = 283 \text{ nm}$, the resistivity was $1.2 \times 10^{-3} \Omega \text{ cm}$. The lower resistivity for the thicker film indicates a change in the microstructure, such as larger grain size and/or different properties at the grain boundaries.

B. Optical constants in the luminous range

The well-known envelope method^{55–58} was used to evaluate the spectral refractive index $n(\lambda)$ and extinction coefficient $k(\lambda)$. Transmission spectra, such as those in Fig. 12, show maxima and minima due to optical interference. In the method used here, the optical constants were determined

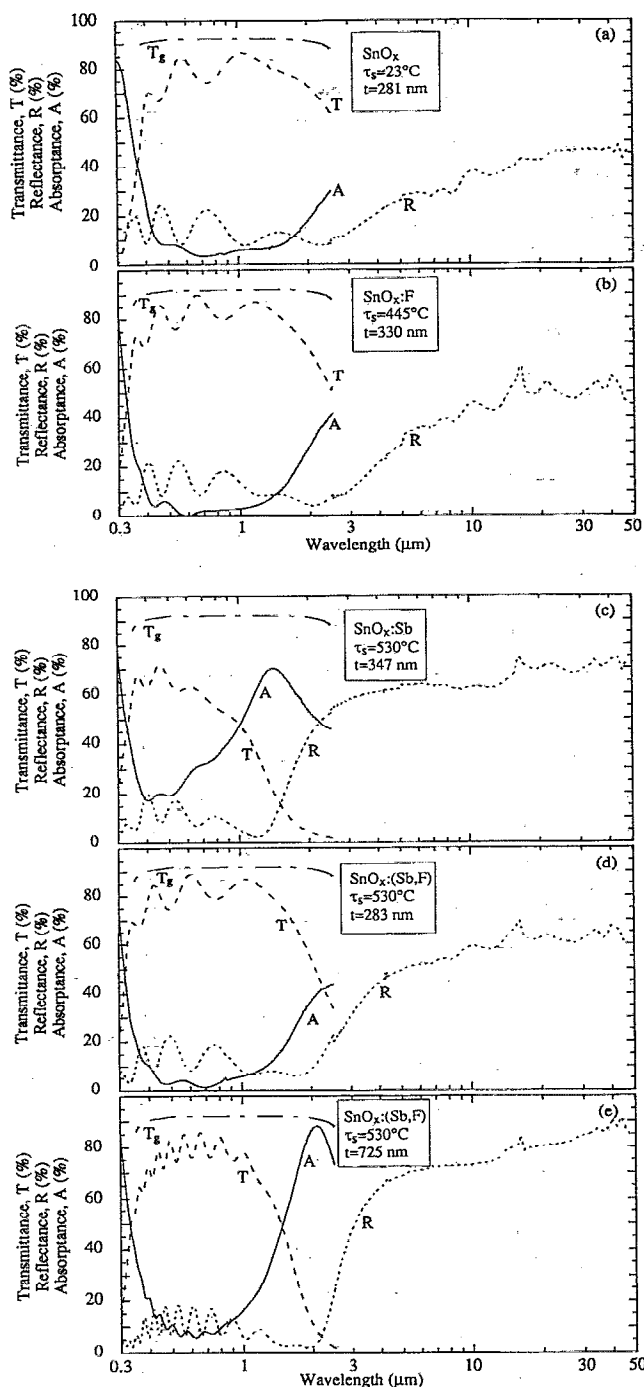


FIG. 12. Spectral transmittance, reflectance, and absorbance for tin-oxide-based films. The insets show doping species, substrate temperature during sputtering τ_s , and film thickness t . The transmittance through an uncoated substrate is given by the curves designated T_g .

from envelope curves denoted $T_{\max}(\lambda)$ and $T_{\min}(\lambda)$, drawn through these maxima and minima. The method is suitable in the case of weak absorption, $k^2 \ll n^2$, which prevails in the luminous range for tin-oxide-based films. The refractive index is given by⁵⁵

$$n = [N + (N^2 - n_0^2 n_1^2)^{1/2}]^{1/2}, \quad (4)$$

with

$$N = \frac{n_0^2 + n_1^2}{2} + 2n_0 n_1 \frac{T_{\max} - T_{\min}}{T_{\max} T_{\min}}, \quad (5)$$

where n_0 is the refractive index of air and n_1 the refractive index of the substrate. The thickness of the film can be calculated from two maxima or minima using

$$t = \frac{M \lambda_1 \lambda_2}{2[n(\lambda_1) \lambda_2 - n(\lambda_2) \lambda_1]}, \quad (6)$$

where M is the number of oscillations between the two extrema occurring for λ_1 and λ_2 and with $n(\lambda_1)$ and $n(\lambda_2)$ being the corresponding refractive indices. The extinction coefficient can be calculated from⁵⁵

$$\exp\left(-\frac{4\pi k t}{\lambda}\right) = \frac{(n + n_0)(n_1 + n)[1 - (T_{\max}/T_{\min})^{1/2}]}{(n - n_0)(n_1 - n)[1 + (T_{\max}/T_{\min})^{1/2}]}. \quad (7)$$

The films analyzed by us were deposited onto quartz substrates using optimized sputter parameters. Thus τ_s was 530 °C for SnO_x , $\text{SnO}_x:\text{Sb}$, and $\text{SnO}_x:(\text{Sb},\text{F})$ films, whereas τ_s was 445 °C for $\text{SnO}_x:\text{F}$. The films were $\sim 500 \pm 100$ nm thick and produced a sufficient number of maxima and minima in the transmittance spectra in order to allow the envelope method to be applied with convenience.

Figure 13 shows the refractive index and extinction coefficient in the $0.4 < \lambda < 0.8$ μm range for four differently doped tin-oxide-based films. These films were produced with the optimized sputter parameters for SnO_x , $\text{SnO}_x:\text{Sb}$ (4 at. %), $\text{SnO}_x:\text{F}$ (3 fl. %), and $\text{SnO}_x:[\text{Sb}(2 \text{ at. } \%), \text{F}(3 \text{ fl. } \%)]$. In part (a) it can be seen that the films are characterized by $1.90 < n < 2.0$, except for the $\text{SnO}_x:\text{Sb}$ (4 at. %) film which shows a decreasing n with increasing λ , from $n = 2.04$ at $\lambda = 0.4$ μm to $n = 1.84$ at $\lambda = 0.8$ μm . A similar decrease of n was observed for all Sb-doped films and became more pronounced with higher C_{Sb} . Figure 13(b) indicates that k is of the order of 10^{-2} in the luminous range.

Table IV lists n and k at $\lambda = 0.57$ μm for ten differently doped films. A slight decrease of n is observed when the doping concentrations of Sb and F are increased. This is in agreement with earlier published results for tin oxide films.^{49,59} From Table IV it is apparent that k increases with increasing C_{Sb} , whereas k is about the same for the different fluorine concentrations of concern here. These data are in accordance with the results for A_{lum} reported earlier in Sec. III B.

C. Band gaps

In the regime of fundamental absorption and if $k^2 \ll n^2$, the transmittance can be approximated by⁶⁰

$$T \approx \exp\left(-\frac{4\pi k t}{\lambda}\right). \quad (8)$$

Optical band gaps were then calculated from the general relation^{61,62}

$$\alpha h \nu \propto (h \nu - E_g)^\eta, \quad (9)$$

where $\alpha = 4\pi k/\lambda$ is the absorption coefficient, h is Planck's constant, ν is frequency, E_g is band gap, and η is a constant

TABLE III. Parameters for five different optimized tin-oxide-based films. Data are given for substrate temperature (τ_s), oxygen gas flow (Γ_{O_2}), CF_4 gas flow (Γ_{CF_4}), antimony concentration (C_{Sb}), film thickness (t), resistivity (ρ_{dc}^*), resistance/square (R_{sq}), deposition rate (r), luminous transmittance (T_{lum}), luminous absorbance (A_{lum}), infrared reflectance (R_{IR}), free-electron concentration (n_H), and mobility (μ_H).

Film material	τ_s (°C)	Γ_{O_2} (fl. %)	Γ_{CF_4} (fl. %)	C_{Sb} (at. %)	t (nm)	ρ_{dc}^* (Ω cm)	R_{sq} (Ω)	r (nm/min)	T_{lum} (%)	A_{lum} (%)	R_{IR} (%)	n_H (cm ⁻³)	μ_H (cm ² /V s)
SnO _x	23	12.2	281	3.6×10^{-3}	128	50.6	81.2	7.0	30–45	0.16×10^{21}	19.7
SnO _x :F	445	12.0	4.0	...	330	2.8×10^{-3}	86	41.2	80.2	1.3	40–50	0.15×10^{21}	13.8
SnO _x :Sb	530	15.4	...	8.0	347	1.3×10^{-3}	38	49.6	62.8	23.5	60–70	0.63×10^{21}	5.8
SnO _x :(Sb,F)	530	12.8	3.0	2.0	283	1.2×10^{-3}	41	35.4	83.0	3.5	60–70	0.23×10^{21}	18.9
SnO _x :(Sb,F)	530	12.4	3.0	2.0	725	9.1×10^{-4}	12.5	36.3	79.7	7.5	70–90

taking the values $\frac{1}{2}$, $\frac{3}{2}$, 2, or 3 depending whether the transitions are direct allowed, direct forbidden, indirect allowed, or indirect forbidden, respectively.

Thin films often show a small band-gap widening, and the absorption edge moves to a shorter wavelength than that of the bulk material. However, when SnO₂ is doped and n_H increases, a substantial band-gap widening is expected. This phenomenon is important in connection with window coatings, since a widening of the band gap helps to avoid unwanted absorption in the luminous spectral range.

Figure 14 shows $(\alpha h\nu)^2$ versus $h\nu$ for some of the films listed in Table IV. A linear extrapolation towards zero absorption gives E_g corresponding to direct allowed transitions. The values obtained for E_g are given in Table IV. The minimum direct allowed transition of undoped SnO₂ is at 3.75 eV.⁶³ By comparing E_g for films with different n_H values, it is evident that band-gap widening occurs with increasing n_H . This effect is also illustrated in Fig. 15. We obtained E_g values ranging from 4.06 to 4.45 eV in energy, or from 0.305 to 0.279 μ m in wavelength. Similar results have been ob-

tained for spray deposited SnO_x, SnO_x:F, and SnO_x:Sb films.⁶⁴

Equation (9) is commonly used to derive band gaps for heavily doped semiconductors. However, the result obtained from this formula is only an approximation of the true band gap. The application of Eq. (9) is close to correct for direct allowed transitions to an empty parabolic conduction band,⁶¹ but for a heavily doped semiconductor, such as the tin-oxide-based films analyzed here, it is not correct³ since the lowest states in the conduction band are blocked and transitions can take place only to energies above the Fermi energy. The band gaps obtained by plotting $(\alpha h\nu)^2$ versus $h\nu$ are expected to be somewhat smaller than the physically correct band gap.⁶⁵ This effect was observed³ in work on In₂O₃:Sn films.

V. STRUCTURAL AND COMPOSITIONAL ANALYSIS

A. X-ray diffraction

X-ray diffraction (XRD) investigations of the tin-oxide-based films were made with a Philips PW 1130/00 diffractometer, operated with Cu K_α as the radiation source at 40 kV and 20 mA. ASTM index cards were used as references for the crystallographic data. XRD studies were made on several series of samples optimized with respect to Γ_{O_2} for a low ρ_{dc}^* . The object was to see whether there were any characteristic structural properties of such films.

Figure 16 shows typical XRD results for films of SnO_x, SnO_x:F, SnO_x:Sb, and SnO_x:(Sb,F). Each panel illustrates XRD intensities for five samples produced with different magnitudes of Γ_{O_2} . The thick curves pertain to the films with lowest ρ_{dc} . It is interesting to note that the XRD peak at 33.9°, corresponding to the (101) plane in SnO₂, shows a maximum for the films with the lowest resistivity for all kinds of doping. Similar results were reported for sputtered SnO₂:Sb by Suzuki and Mizuhashi.¹⁴ Other strong diffraction peaks lie at 26.6° (110), 37.9° (200), 51.7° (211), and 57.8° (002), but their maxima in intensity do not show the same regularity as for the (101) peak.

In bulk SnO₂, the ASTM data (card number 21-1250) yield that the diffracted intensities for the (110), (101), (200), (211), and (002) peaks have the relative intensities 100, 80, 25, 65, and 8, respectively. Comparing these intensities with those in Fig. 16, it is clear that for sputtered tin-oxide-based films there is a deviation from the ASTM data. There is also

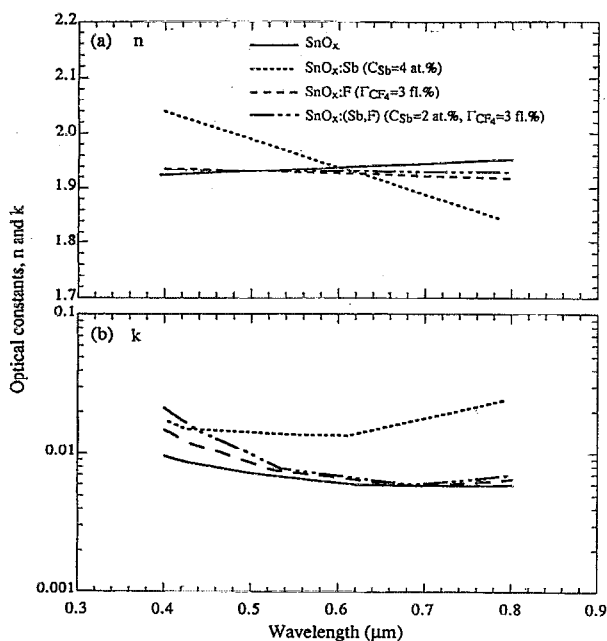


FIG. 13. Spectral optical constants, n and k , for tin-oxide-based films of the four types shown as curve designations.

TABLE IV. Optical constants n and k at $0.57\ \mu\text{m}$ and band gap E_g obtained by use of the envelope method for tin-oxide-based films produced by sputtering from different target materials in different plasmas. The free-electron concentration n_H was obtained from Hall-effect measurements.

Film material	n at $0.57\ \mu\text{m}$	k at $0.57\ \mu\text{m}$	E_g (eV)	n_H ($10^{21}\ \text{cm}^{-3}$)
SnO_x	1.94	0.0064	4.06	0.015
$\text{SnO}_x:\text{Sb}$ (2 at. %)	1.95	0.0070	4.17	0.35
$\text{SnO}_x:\text{Sb}$ (4 at. %)	1.96	0.0136	4.40	0.54
$\text{SnO}_x:\text{Sb}$ (8 at. %)	1.92	0.0196	4.41	0.80
$\text{SnO}_x:\text{F}$ (1.5 fl. %)	1.96	0.0079	4.10	0.09
$\text{SnO}_x:\text{F}$ (3 fl. %)	1.93	0.0070	4.14	0.15
$\text{SnO}_x:\text{F}$ (6 fl. %)	1.91	0.0067	4.11	0.13
$\text{SnO}_x:[\text{Sb}$ (2 at. %), F (3 fl. %)]	1.94	0.0073	4.07	0.23
$\text{SnO}_x:[\text{Sb}$ (4 at. %), F (3 fl. %)]	1.96	0.0105	4.41	0.39
$\text{SnO}_x:[\text{Sb}$ (8 at. %), F (3 fl. %)]	1.87	0.0275	4.45	0.79

a strong variation in the intensities of the diffraction peaks with varying Γ_{O_2} . A change in the relative intensities could be a sign of preferential orientation, and in the case of an increasing intensity of the (101) peak this would indicate that the (101) planes are parallel to the surfaces of the film. This is not a unique interpretation, though, and it is also possible that the structure factor of the crystal unit cell is changed when Γ_{O_2} is altered.

The XRD pattern for a tin oxide film doped with Sb, shown in Fig. 16(c), deviates from the other patterns and shows only two strong peaks for each film. This may suggest that the tendency for having a preferred direction of growth or a change in the structure factor is stronger with Sb doping than for other types of doping.

Indications can be found in the literature that the (101) peak is always relatively strong for tin oxide films with low resistivity, irrespective of deposition techniques and doping species. In most cases this feature has not been mentioned as a sign of low resistivity, with the exception being the sputtered $\text{SnO}_x:\text{Sb}$ films reported on in Ref. 14. Examples of other published works indicating strong (101) peaks at low

ρ_{dc} include Refs. 34 and 66 for evaporated films, Refs. 67 and 68 for films made by chemical-vapor deposition, and Refs. 69 and 70 for spray deposited films.

B. Transmission electron microscopy

Transmission electron microscopy (TEM) was carried out at 200 kV using a JEOL 2000FX TEM/STEM instrument. The specimens were $\sim 100\ \text{nm}$ thick tin oxide films sputtered onto carbon-covered copper grids. The specimens were subsequently ion-beam thinned to a final thickness of about 20–30 nm. Electron microscopy was performed mainly using bright field imaging. Results from electron diffraction were compared with ASTM data in order to evaluate the structure.

TEM was employed to study the microstructure of tin oxide films deposited at various substrate temperatures and having different dopant concentrations. In most of the analyses, Γ_{O_2} was kept at Γ^* . Electron diffraction was used to obtain patterns such as the one in Fig. 17, referring to a SnO_x film prepared at $\tau_s=530\ ^\circ\text{C}$. The various rings can be assigned to specific (hkl) indices (ASTM card 21-1250), proving that the structure is tetragonal. Bright field images were used to determine the linear extents of the grains; specific TEM images, with corresponding electron-diffraction patterns, are given in Figs. 18–22.

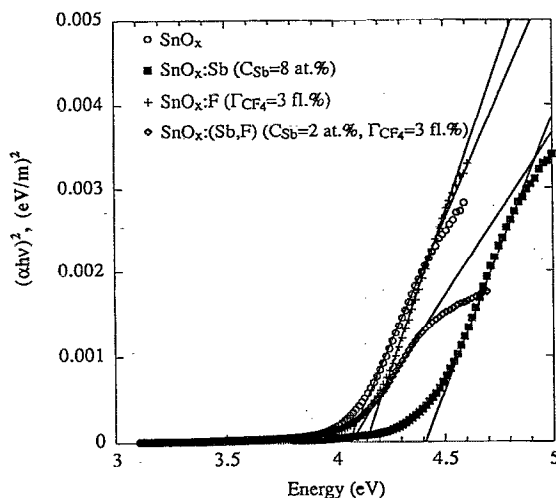


FIG. 14. $(\alpha h\nu)^2$ vs photon energy for tin-oxide-based films. Different symbols pertain to films of the shown types. Straight lines represent extrapolations used for obtaining optical band gaps.

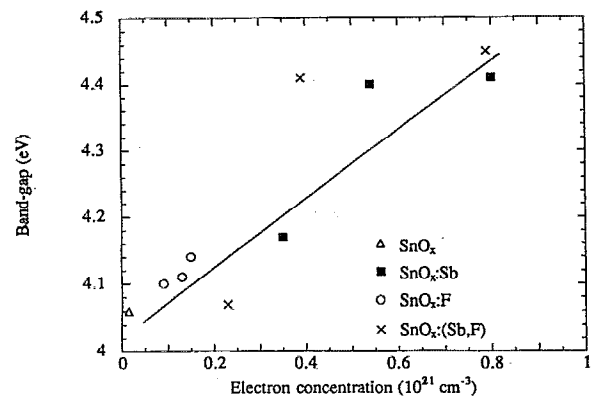


FIG. 15. Optical band gap vs electron concentration for tin-oxide-based films with the indicated doping species.

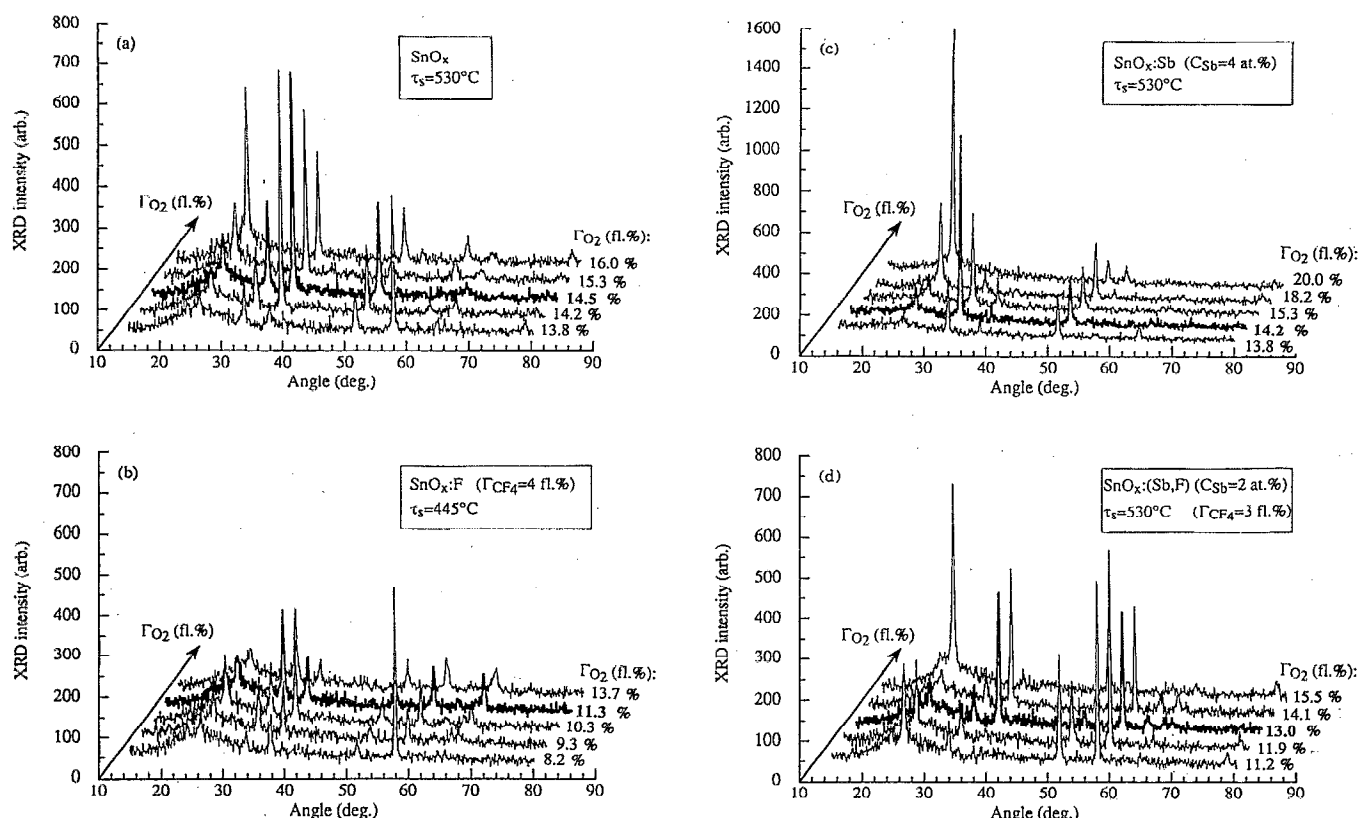


FIG. 16. X-ray-diffracted intensity vs angle for tin-oxide-based films. The insets show doping species, antimony content in the target C_{Sb} , relative carbon tetrafluoride content in the sputter plasma Γ_{CF_4} , and substrate temperature during sputtering τ_s . The curves pertain to the shown values of the relative oxygen content Γ_{O_2} . Bold curves refer to samples prepared at Γ^* .

Figure 18 shows micrographs and corresponding diffraction patterns for SnO_x films made at three different substrate temperatures. The structure is polycrystalline, and it can be seen that the grain size increased with increasing temperature from 6–10 nm at $\tau_s = 370^\circ C$ to 8–16 nm at $\tau_s = 530^\circ C$. The rings in the diffraction patterns were more distinct when τ_s was increased, pointing at a higher degree of crystallinity.

The micrograph in Fig. 19(a) refers to a SnO_x film deposited with $\Gamma_{O_2} > \Gamma^*$, deposited with $\Gamma_{O_2} < \Gamma^*$ and $\tau_s = 530^\circ C$. The grain sizes were

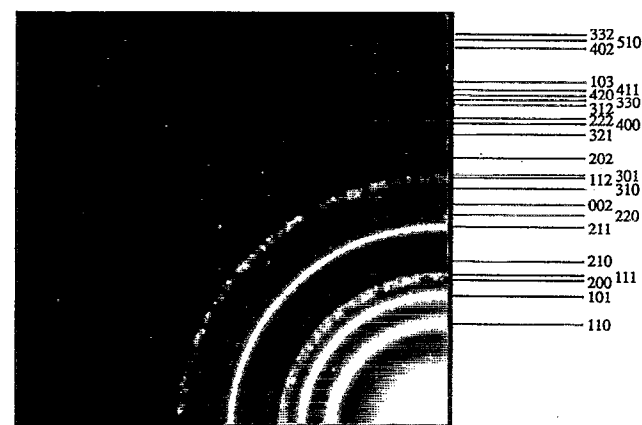
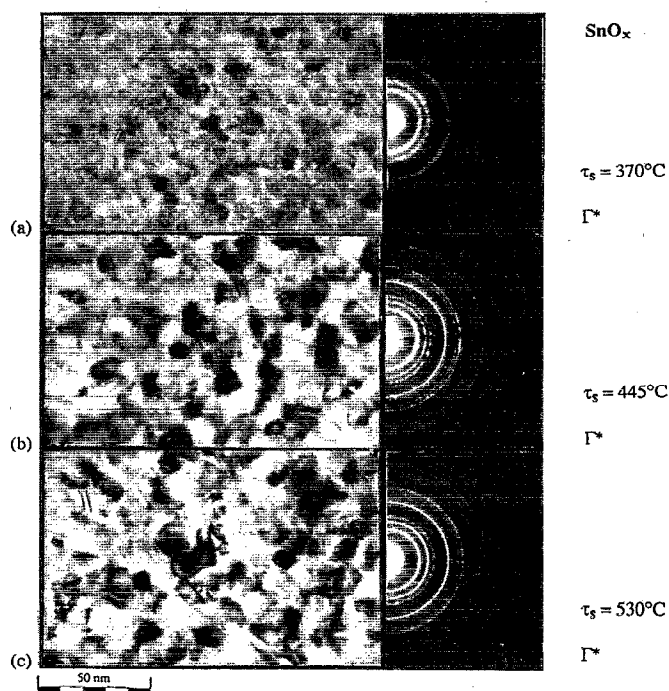


FIG. 17. Selected area diffraction pattern for a nonstoichiometric tin oxide film. The rings can be assigned to the shown (hkl) indices.

FIG. 18. Transmission electron micrographs and electron-diffraction patterns for nonstoichiometric tin oxide films deposited at the optimized relative oxygen content onto substrates with the shown temperature τ_s .

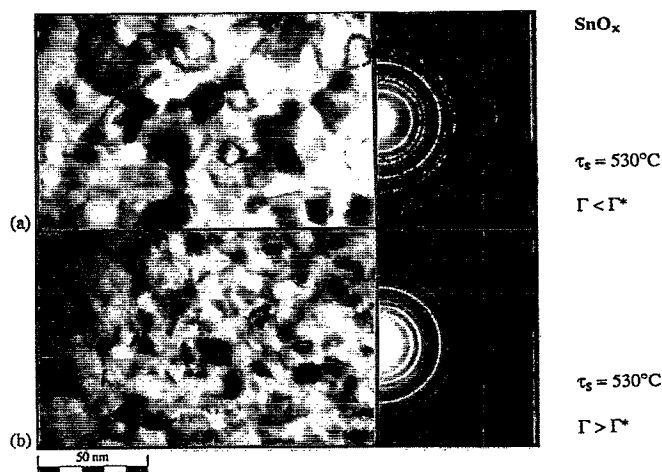


FIG. 19. Transmission electron micrographs and electron-diffraction patterns for nonstoichiometric tin oxide films deposited at the shown relative oxygen content Γ_{O_2} onto substrates at 530 °C.

reported on in Fig. 19(b), had grain sizes of 6–14 nm. At Γ^* , the grain size was 8–16 nm, as pointed out above. These data indicate that the grain size decreases with increasing Γ_{O_2} . The diffraction patterns showed that the ring corresponding to the (101) plane was comparatively strong for the film prepared at Γ^* (i.e., for the SnO_x film with the lowest resistivity).

The electron-diffraction patterns were recorded with the surface perpendicular to the incident electron beam. With

this geometry one obtains information of the crystal planes that are perpendicular to the film surface, and thus it is possible to obtain knowledge that is complementary to the XRD data presented above. The increased intensity assigned to the (101) planes, observed with both electron diffraction and XRD, indicates that the change in the relative intensities is influenced by a change of the structure factor. If preferred crystallographic orientation were the only operating mechanism, an increase in the XRD pattern would correspond to a decrease in the intensity for the corresponding ring in the electron-diffraction pattern.

Figures 20–22 show micrographs of films doped with Sb and/or F. The grain size of the Sb-doped films (Fig. 20) was largest with $C_{\text{Sb}}=4$ at. % (14–30 nm). When C_{Sb} was further increased to 8 at. %, the grain size decreased to 6–20 nm. A possible reason for this is that inclusions of Sb_2O_3 and Sb_2O_5 are present in the film with $C_{\text{Sb}}=8$ at. %. Such inclusions would be expected to hinder the growth of the tin oxide grains. Antimony oxide inclusions are likely to be responsible for the bluish color observed in heavily Sb-doped SnO_2 films, as mentioned earlier.

For the F-doped films reported on in Fig. 21, the grain sizes were rather independent of the magnitude of Γ_{CF_4} . Specifically, the grain sizes were 6–10 nm for Γ_{CF_4} being 1.5 and 3 fl. %, and 6–14 nm for Γ_{CF_4} being 6 fl. %.

The studied $\text{SnO}_x:(\text{Sb},\text{F})$ films (Fig. 22) were deposited with a constant Γ_{CF_4} of 3 fl. %. The grain sizes are very close to those obtained for the purely Sb-doped films, except for the one with $C_{\text{Sb}}=4$ at. % which showed a smaller grain size when F was added.

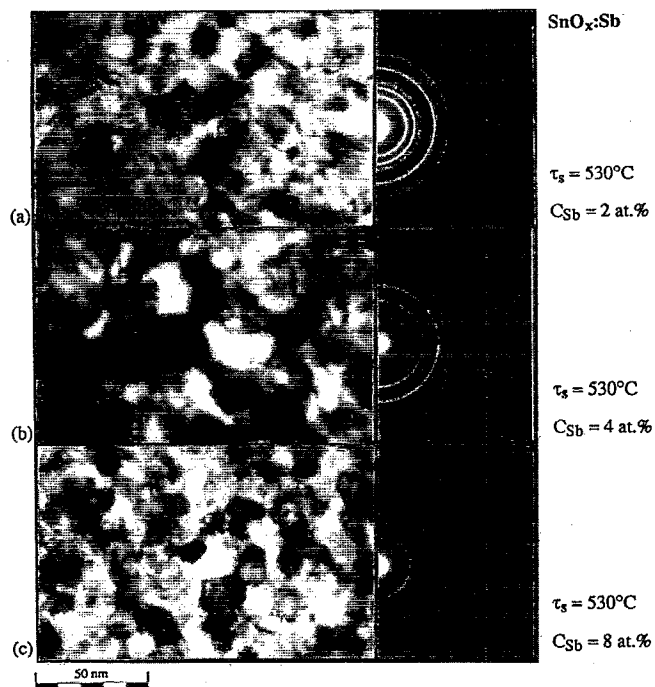


FIG. 20. Transmission electron micrographs and electron-diffraction patterns for $\text{SnO}_x:\text{Sb}$ films deposited at the optimized relative oxygen content onto substrates at 530 °C. The shown antimony contents C_{Sb} were used.

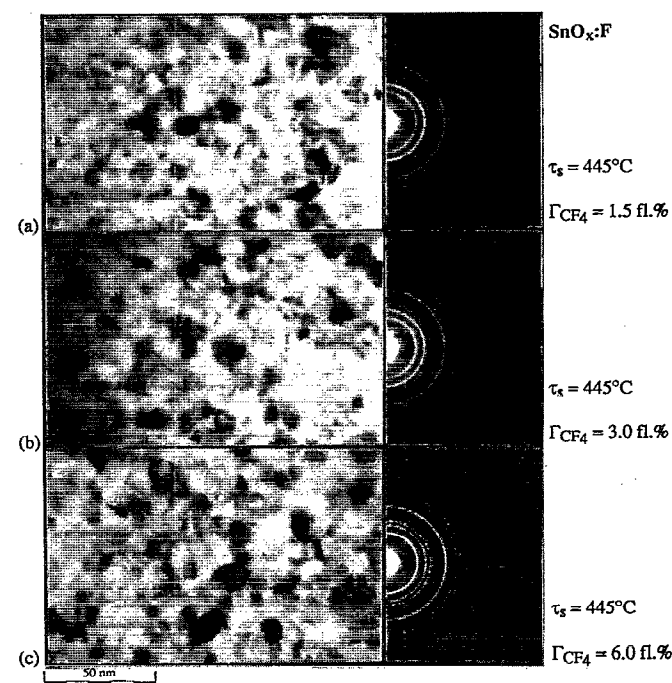


FIG. 21. Transmission electron micrographs and electron-diffraction patterns for $\text{SnO}_x:\text{F}$ films deposited at the optimized relative oxygen content onto substrates at 445 °C. The shown fluorine flow rates Γ_{CF_4} were used.

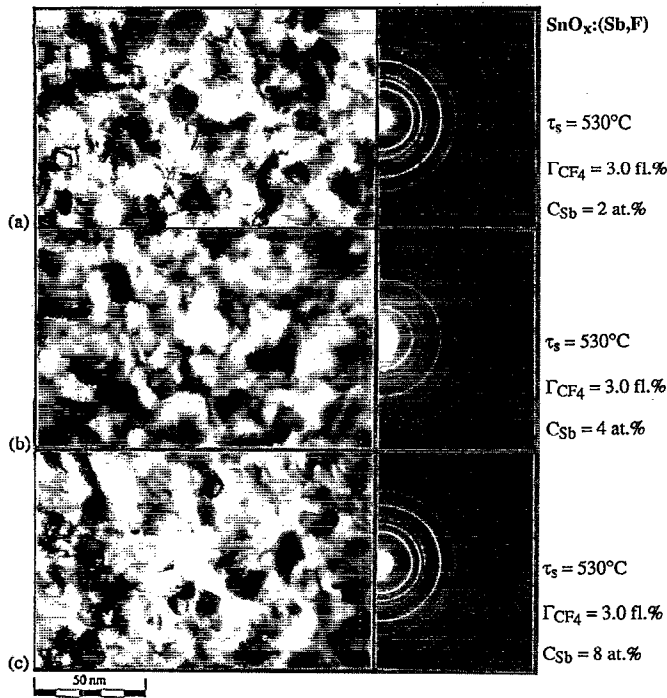


FIG. 22. Transmission electron micrographs and electron-diffraction patterns for $\text{SnO}_x(\text{Sb},\text{F})$ films deposited at the optimized relative oxygen content onto substrates at 530°C . The shown antimony contents C_{Sb} and fluorine flow rate were used.

The (110), (101), and (200) reflections in the electron-diffraction patterns show the highest intensity for all films. Their relative intensities changed when the deposition conditions were altered. This observation, in combination with the XRD results discussed above, suggests that the structure factor—and perhaps also the degree of preferential orientation—are strongly sensitive to the concentration of F and Sb as well as to the oxygen content.

It is illuminating to compare grain sizes for tin-oxide-based thin films prepared with different deposition techniques. There are literature results for films made by CVD,^{71,72} spray pyrolysis,^{50,71,73,74} evaporation,³³ and sputtering^{11,14} that can be directly compared to the results reported in the present work. The results reported for CVD, spray pyrolysis, and evaporation suggest two to five times larger grain sizes than those reported for sputtered films. The grain size influences the electrical mobility and conductivity of thin films, and the small grains in sputtered tin oxide films offer a plausible explanation of the lower conductivity for such films than for films made by several other deposition techniques.

VI. THEORETICAL ANALYSIS

A. Model for the optical properties

There are different theoretical models for describing the electromagnetic properties of doped wide band-gap semiconductors such as $\text{In}_2\text{O}_3:\text{Sn}$, $\text{ZnO}:\text{Al}$, SnO_x , $\text{SnO}_x:\text{F}$, and $\text{SnO}_x:\text{Sb}$. Here we will make a comparison between experimental results, obtained for tin oxide films doped with oxy-

gen vacancies or with Sb and/or F with results from a theoretical model used in earlier work of this laboratory^{3–5} and with results from the simple Drude model.

The frequency dependent dielectric function $\epsilon(\omega)$ of a heavily doped semiconductor in most cases can be expressed as a sum of contributions from valence electrons (VE), free carriers (FC), and polar optical phonons (PH) according to³⁶

$$\epsilon = 1 + \chi^{\text{VE}} + \chi^{\text{FC}} + \chi^{\text{PH}}, \quad (10)$$

where χ denotes a susceptibility in SI units. Well away from the semiconductor band gap (in the ultraviolet) and phonon resonances (in the midthermal range), one can write

$$\epsilon(\omega) = \epsilon_\infty + \chi^{\text{FC}}(\omega), \quad (11)$$

where ϵ_∞ is the high-frequency dielectric constant.

For doped tin oxide films, the free carriers are electrons. The free-electron contribution is conveniently discussed in terms of a dynamic resistivity

$$\rho(\omega) = \rho_1(\omega) + i\rho_2(\omega), \quad (12)$$

which is related to the free-electron susceptibility by the general relation

$$\chi^{\text{FC}}(\omega) = i/\epsilon_0\omega\rho(\omega), \quad (13)$$

with ϵ_0 being the permittivity of free space.

According to the classical one-electron model by Drude, the frequency dependent resistivity can be expressed by

$$\rho^D(\omega) = \frac{1}{\epsilon_0\omega_p^2\tau} - i\frac{\omega}{\epsilon_0\omega_p^2}, \quad (14)$$

$$\omega_p^2 = \frac{n_e e^2}{\epsilon_0 m_c^*}, \quad (15)$$

where ω_p is the plasma frequency, τ the relaxation time, n_e the free-electron density, and m_c^* the effective conduction-band mass. The first term in Eq. (14) represents the scattering of the free electrons, while the second term stems from the inertia of the free electrons; it vanishes in the dc case wherein

$$\rho^D(0) = \frac{1}{\epsilon_0\omega_p^2\tau}. \quad (16)$$

It should be stressed that the Drude theory is highly simplified and introduces electron scattering via a phenomenological frequency independent parameter τ .

Detailed and quantitative expressions for $\rho(\omega)$ in the case of different scattering mechanisms can be obtained from solutions of the Boltzmann transport equation⁷⁵ as well as from the equivalence of Joule heat and energy loss.⁷⁶ The latter approach gives the expression³⁶

$$\rho^{\text{IIS}}(\omega) = \frac{Z^2 N_i}{6\pi^2 \epsilon_0 n_e^2 \omega} \int_0^\infty k^2 dk \left(\frac{1}{\epsilon(\mathbf{k}, \omega)} - \frac{1}{\epsilon(\mathbf{k}, 0)} \right) - i\frac{\omega}{\epsilon_0\omega_p^2} \quad (17)$$

for ionized impurity scattering (IIS) in a nonpolar semiconductor with Coulomb-type ion potentials. Here Z is the charge of the impurities, N_i the impurity density, and $\epsilon(\mathbf{k}, \omega)$ the dielectric function of the free-electron gas. It is possible to calculate $\epsilon(\mathbf{k}, \omega)$ for a degenerate electron gas from the

random-phase approximation;⁷⁷ explicit formulas were given in Ref. 3. We note that the theory regards independent point charges, whereas in reality we have ions with a spatial extension and with a probability of being clustered at the pertinent doping levels.

The derivation of Eq. (17) does not account for displacement polarization of the atoms and is not easily generalized to incorporate this effect.⁷⁸ However, for a polar semiconductor the dynamic resistivity can be computed from the Kubo formalism and diagrammatic perturbation theory.⁷⁹ This latter theory was used to explain band-gap widening in ZnO:Al⁸⁰ and to evaluate the role of displacement polarization on free-electron properties.⁷⁸ Theoretically, one expects that the full computation should yield a magnitude of $\rho(\omega)$ that is lower than the one for a nonpolar model by a factor of 2 or 3. Empirically, however, computations based on Eq. (17) are in good agreement with experimental results for In₂O₃:Sn,³ ZnO:Al,⁴ and SnO_x.⁵

Below we will use the nonpolar expressions of $\rho^{\text{IIS}}(\omega)$ in Eq. (17) and compare computed results with experimental data. We will also compare them with results from the Drude model having a constant τ in Eq. (14).

Once $\epsilon(\omega)$ was obtained, transmittance, reflectance, and absorbance were computed from Fresnel's formulas⁸¹ for a thin film on a thick substrate. Specifically, the substrate was characterized by known dielectric functions for Corning 7059 glass at $\lambda < 2.5 \mu\text{m}$ (Ref. 82) and for SiO₂ at $\lambda > 2.5 \mu\text{m}$.³⁷

B. Comparison of experimental and theoretical results on the optical properties

The purpose of this section is to compare experimental and theoretical results for T , R , and A and to draw conclusions regarding the scattering mechanisms in doped tin oxide films. Detailed analyses were performed for four films doped with either oxygen vacancies, Sb, F, or Sb+F.

A number of input parameters need to be specified before the calculations can be carried out. Regarding the dynamic resistivity for ionized impurity scattering, they are n_e , N_i , m_c^* , Z , and ϵ_∞ . We take n_e to be the value obtained from Hall-effect measurements (earlier denoted n_H). Doping with Sb and/or F is considered to generate one extra conduction electron per incorporated foreign atom, which suggests singly ionized scattering centers, i.e., $Z=1$ and thereby $N_i=n_e$. In the case of SnO_x, doubly ionized oxygen vacancies are assumed to serve as donors.³⁸ Thus we put $Z=2$ and $N_i=n_e/2$. The magnitude of m_c^* was set equal to $0.38m_0$ with m_0 being the free-electron mass, which is the value used in Ref. 83 and close to the measured value $0.39m_0$ in Ref. 44. The high-frequency dielectric constant was taken to be^{38,84–86} $\epsilon_\infty=4$. The dynamic resistivity calculated for low frequencies, denoted $\rho^{\text{IIS}}(0)$, is readily compared with the measured dc resistivity ρ_{dc} .

The Drude model based on Eq. (14) has the input parameters n_e , m_c^* , τ , and ϵ_∞ . We specified τ by putting $\rho^D(0)=\rho_{dc}$ and used the same values for the other parameters as in the computation for ionized impurity scattering.

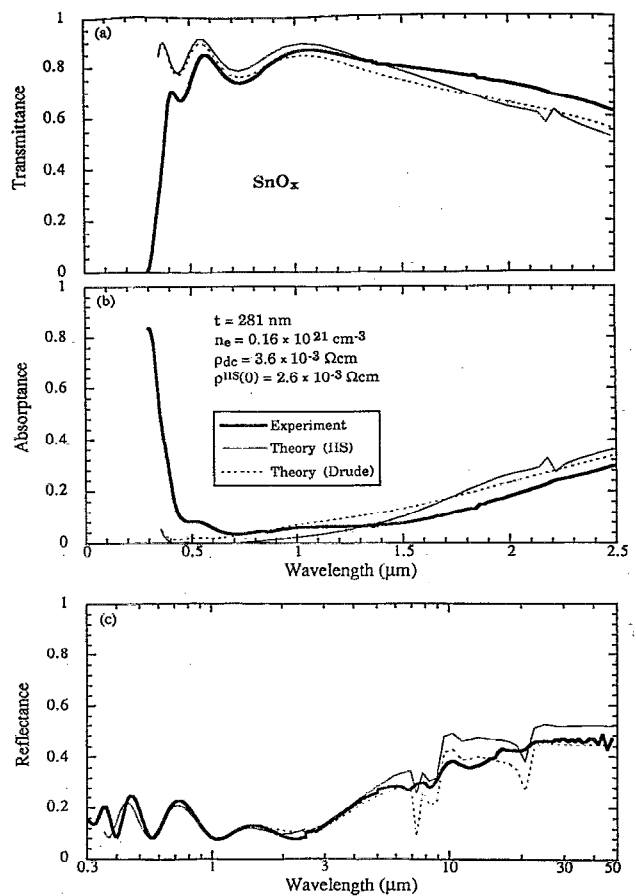


FIG. 23. Spectral transmittance, absorbance, and reflectance for a nonstoichiometric tin oxide film as measured and as calculated from a theory encompassing IIS and from the Drude theory. The experimental sample is characterized in the first line of Table III. Resistivity values needed in the calculations, ρ_{dc} and $\rho^{\text{IIS}}(0)$, are given in the figure.

Figures 23–26 show calculated spectra for transmittance, absorbance, and reflectance. We present T and A for $0.3\text{--}2.5 \mu\text{m}$, whereas R is given for $0.3\text{--}50 \mu\text{m}$. The limited wavelength range for T and A is due to the fact that Corning 7059 glass is not transparent in the thermal infrared. We note a qualitative agreement between experimental and theoretical curves, but quantitative differences exist.

For SnO_x, Fig. 23 shows that the experimental transmittance is lower than the calculated one for $\lambda < 0.5 \mu\text{m}$, whereas the experimental absorbance is higher than the calculated one. A similar tendency is apparent for SnO_x:Sb, as found from Fig. 25. These phenomena can be understood as results of stoichiometry deviations, being SnO-like inclusions in SnO_x and inclusions of Sb₂O₃ and Sb₂O₅ in SnO_x:Sb. The inclusions are not encompassed by the theories, and a proper analysis would require effective-medium theory, which is outside the scope of the present paper. The failure of the theories to capture the phonon induced structure measured in the thermal infrared is by no means unexpected since the composition of the glass substrate deviates significantly from SiO₂.

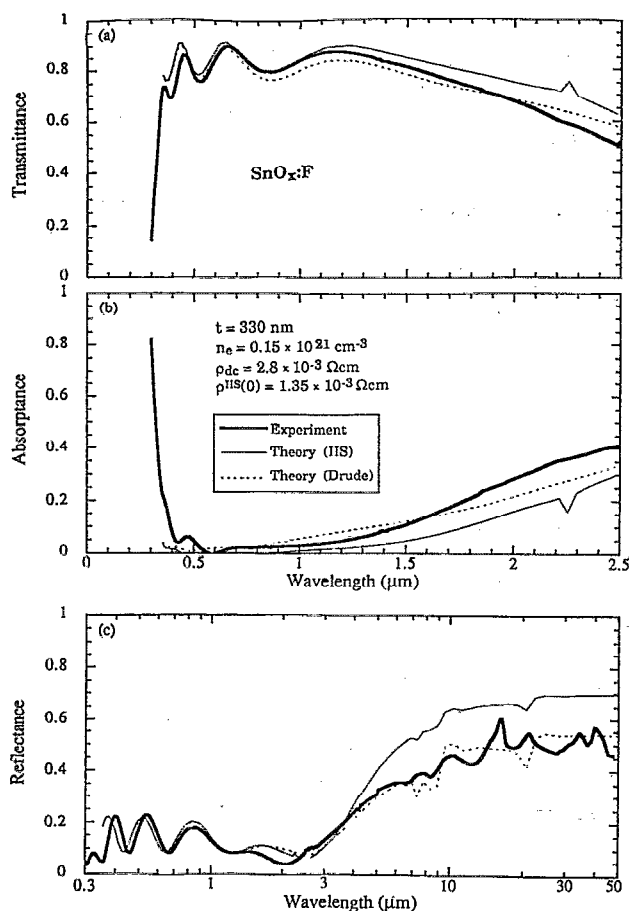


FIG. 24. Spectral transmittance, absorbance, and reflectance for a fluorine-doped tin oxide film as measured and as calculated from a theory encompassing IIS and from the Drude theory. The experimental sample is characterized in the second line of Table III. Resistivity values needed in the calculations, ρ_{dc} and $\rho^{IIS}(0)$, are given in the figure.

At wavelengths up to those where the reflectance increases strongly—i.e., for $\omega > \omega_p$ —the theory for ionized impurity scattering and the Drude theory are about equally successful in reproducing the experimental data. However, at longer wavelengths ($\omega < \omega_p$) the Drude theory is superior. The reason for this is that the infrared reflectance basically depends on the dc resistivity, and since the measured ρ_{dc} was used as an input parameter in the Drude calculations, a good agreement is, in fact, expected. In the case of ionized impurity scattering, however, the resistivity in the infrared region was obtained as a result from the calculations, and it turns out that $\rho^{IIS}(\omega)$ is lower than the measured ρ_{dc} for all investigated films. Pertinent values of these parameters are given in Figs. 23–26. The relative difference between the two quantities is smallest for the film doped by oxygen vacancies (Fig. 23), which may explain why the agreement between the experimental and theoretical reflectance is better for the SnO_x film than for the other films.

Our analysis shows unambiguously that $\rho^{IIS}(0) < \rho_{dc}$, which points at the importance of scattering centers other than the ionized impurities. One possible contribution to the scattering of the conduction electrons could be from the grain boundaries. In order to assess whether they are of im-

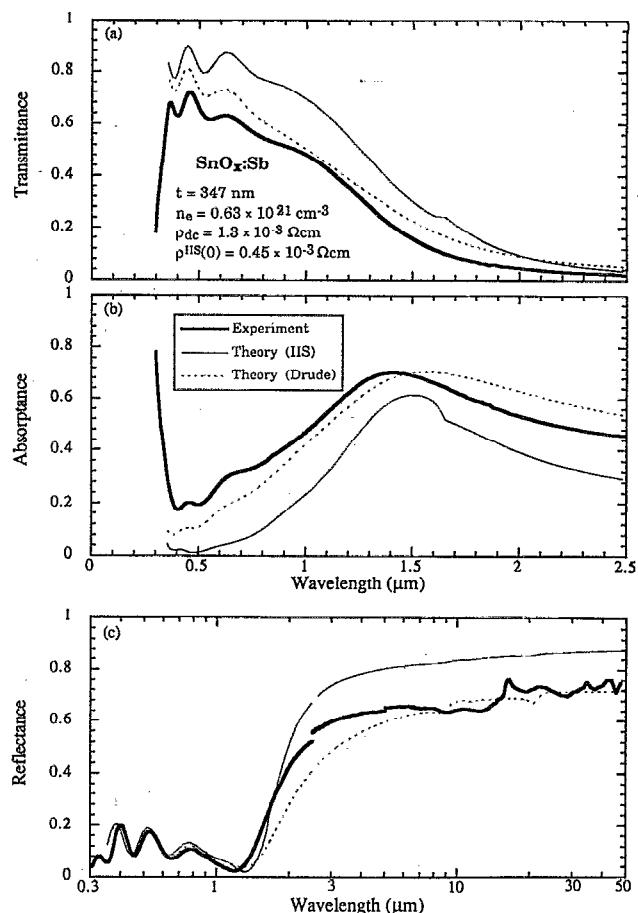


FIG. 25. Spectral transmittance, absorbance, and reflectance for an antimony-doped tin oxide film as measured and as calculated from a theory encompassing IIS and from the Drude theory. The experimental sample is characterized in the third line of Table III. Resistivity values needed in the calculations, ρ_{dc} and $\rho^{IIS}(0)$, are given in the figure.

portance, one can make an estimation of the mean free path l of the conduction electrons from

$$l = \tau v_F, \quad (18)$$

where

$$v_F = \frac{h}{m_c^*} (3\pi^2 n_e)^{1/3} \quad (19)$$

is the Fermi velocity, and compare l with the grain size. By use of the experimentally observed ρ_{dc} , n_e , and Eqs. (14), (15), (18), and (19), one estimates that the mean free path is 3–4 nm. The typical grain sizes of our tin oxide films, as found from electron microscopy, were ~10–20 nm. Our conclusion is that the influence of grain-boundary scattering on the total scattering is not negligible. The part of the resistivity that originates from grain-boundary scattering is expected⁸⁷ to be temperature dependent which, in principle, makes an experimental determination of the grain-boundary contribution feasible. However, our Hall-effect measurements in the 17–295 K range did not indicate any temperature dependence. For the moment we can only state that scattering centers in addition to the ionized impurities have to be considered if a full agreement between experiment and

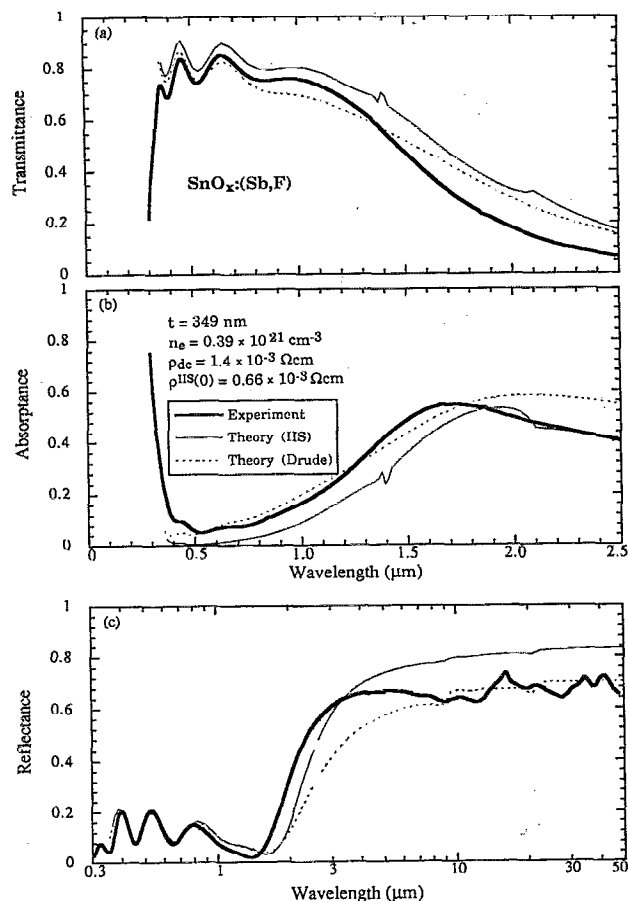


FIG. 26. Spectral transmittance, absorbance, and reflectance for a fluorine plus antimony doped tin oxide film as measured and as calculated from a theory encompassing IIS and from the Drude theory. The experimental sample is characterized by the shown thickness t and electron concentration n_e . Resistivity values needed in the calculations, ρ_{dc} and $\rho^{IIS}(0)$, are given in the figure.

theory for tin-oxide-based films is to be achieved. Future studies have to be carried out in order to elucidate the nature of the full scattering mechanism.

The good agreement between the experiments and the Drude model can be employed for parameterizing optical data. However, since the Drude model is purely phenomenological, it cannot give insights into the actual physical cause of the scattering.

VII. SUMMARY AND CONCLUDING REMARKS

In this paper we have presented a study of tin oxide films doped with oxygen vacancies, F, Sb, or Mo. The films were prepared by reactive rf magnetron sputtering. Among the variously doped tin-oxide-based films made on heated substrates, those incorporating Sb+F showed the lowest resistivity, and optimized deposition parameters gave films with a resistivity as low as $9.1 \times 10^{-4} \Omega \text{ cm}$, a luminous transmittance as high as 80%, a luminous absorbance as low as 7.5%, and an infrared reflectance in the $\sim 70\%$ – 90% range. The substrate temperature was 530°C for these films. Hall-effect measurements showed n -type conduction with electron densities in the 10^{20} – 10^{21} cm^{-3} range. Films doped with

a high concentration of Sb showed the highest electron density. Storing the films in the laboratory for several months did not lead to measurable changes of the electrical properties. We note that 530°C is too high for applications to ordinary window glass, which should not be heated to more than $\sim 450^\circ \text{C}$.

Optical properties, specifically the refractive index n and the extinction coefficient k , were evaluated from spectrophotometric transmittance data. In the luminous range, the films were characterized by $1.90 < n < 2.0$ and $k \sim 10^{-2}$. A slight decrease of n and increase of k was observed when the doping concentrations of Sb and F were increased. In the ultraviolet, the spectrophotometric data were consistent with a band gap due to direct allowed transitions. Band-gap broadening was observed with increasing electron concentration.

X-ray-diffraction investigations showed that the structure factor, and perhaps also the preferred direction of growth, of the sputtered SnO_x films depended on the oxygen content as well as on the specific kind of doping. An x-ray-diffraction peak at 33.9° , corresponding to the crystallographic (101) planes in SnO_2 , showed a maximum in the films with the lowest resistivity for all kinds of doping. Transmission electron microscopy showed different grain sizes in the films depending on oxygen content during sputtering, substrate temperature, and doping species. Grain sizes ranging from 6 to 30 nm were observed.

We modeled the optical and electrical properties from a theory of the complex dynamical resistance due to ionized impurity scattering. This theory allowed us to calculate transmittance, reflectance, and absorbance for tin oxide films doped with either oxygen vacancies or with Sb and/or F. The main conclusion of a comparison between experimental and theoretical data was that ionized impurity scattering is strong, but it is not the only important scattering mechanism. Among the other possible scattering mechanisms, we specifically note grain-boundary scattering.

¹C. G. Granqvist, *Spectrally Selective Surfaces for Heating and Cooling Applications* (SPIE Optical Engineering, Bellingham, 1989); *Large-area Chromogenics: Materials and Devices for Transmittance Control*, edited by C. M. Lampert and C. G. Granqvist (SPIE Optical Engineering, Bellingham, 1990); C. G. Granqvist, in *Materials Science for Solar Energy Conversion Systems*, edited by C. G. Granqvist (Pergamon, Oxford, 1991), p. 106.

²*Display Devices, Topics in Applied Physics*, edited by J. I. Pankove (Springer, Berlin, 1980), Vol. 40.

³I. Hamberg and C. G. Granqvist, *J. Appl. Phys.* **60**, R123 (1986).

⁴Z.-C. Jin, I. Hamberg, and C. G. Granqvist, *J. Appl. Phys.* **64**, 5117 (1988).

⁵B. Stjerna and C. G. Granqvist, *Appl. Phys. Lett.* **57**, 1989 (1990).

⁶B. Stjerna and C. G. Granqvist, *Sol. Energy Mater.* **20**, 225 (1990).

⁷T. Minami, H. Nanto, and S. Takata, *Jpn. J. Appl. Phys.* **27**, L287 (1988).

⁸R. G. Goodchild, J. B. Webb, and D. F. Williams, *J. Appl. Phys.* **57**, 2308 (1985).

⁹F. Demicheli, E. Minetti-Mezzetti, A. Tagliaferro, and E. Tresso, *Nuovo Cimento* **4**, 68 (1984).

¹⁰G. Beensh-Marchwicka, L. Krol-Stepniewska, and A. Miziuk, *Thin Solid Films* **113**, 215 (1984).

¹¹A. De and S. Ray, *J. Phys. D* **24**, 719 (1991).

¹²N. Miyata and H. Kitahata, *Thin Solid Films* **125**, 33 (1985).

¹³H. W. Lehmann and R. Widmer, *Thin Solid Films* **27**, 359 (1975).

¹⁴K. Suzuki and M. Mizuhashi, *Thin Solid Films* **97**, 119 (1982).

- ¹⁵ C. Geoffroy, G. Campet, F. Menil, J. Portier, J. Salardienne, and G. Couturier, *Active Passive Elect. Comp.* **14**, 111 (1991).
- ¹⁶ C. Agashe, B. R. Marathe, M. G. Takwale, and V. G. Bhide, *Thin Solid Films* **164**, 261 (1988).
- ¹⁷ M. N. Islam and M. O. Hakim, *J. Mater. Sci. Lett.* **4**, 1125 (1985).
- ¹⁸ J. C. Manificier, L. Szepessy, J. F. Bresse, and M. Perotin, *Mater. Res. Bull.* **14**, 163 (1979).
- ¹⁹ T. Karlsson, A. Roos, and C.-G. Ribbing, *Sol. Energy Mater.* **11**, 469 (1985).
- ²⁰ I. S. Mulla, H. S. Soni, V. J. Rao, and A. P. B. Sinha, *J. Mater. Sci.* **21**, 1280 (1986).
- ²¹ H. Kaneko and K. Miyake, *J. Appl. Phys.* **53**, 3629 (1982).
- ²² H. H. Afify, R. S. Momtaz, W. A. Badawy, and S. A. Nasser, *J. Mater. Sci.* **2**, 40 (1991).
- ²³ P. Grosse, F. J. Schmitte, G. Frank, and H. Köstlin, *Thin Solid Films* **90**, 309 (1982).
- ²⁴ M. Kojima, H. Kato, and A. Imai, *J. Appl. Phys.* **64**, 1902 (1988).
- ²⁵ N. Srinivasa Murty and S. R. Jawalekar, *Thin Solid Films* **108**, 277 (1983).
- ²⁶ K. B. Sundaram and G. K. Bhagavat, *J. Phys. D* **16**, 69 (1983).
- ²⁷ D. Bélanger, J. P. Dodelet, B. A. Lombos, and J. I. Dickson, *J. Electrochem. Soc.* **132**, 1398 (1985).
- ²⁸ T. P. Chow, M. Ghezzi, and B. J. Baliga, *J. Electrochem. Soc.* **129**, 1040 (1982).
- ²⁹ J. Proscia and R. G. Gordon, *Thin Solid Films* **214**, 175 (1992).
- ³⁰ T. Maruyama and K. Tabata, *J. Appl. Phys.* **68**, 4282 (1990).
- ³¹ W. Luo and Z. Tan, *J. Phys. (Paris) C5*, 773 (1989).
- ³² H. S. Randhawa, M. D. Matthews, and R. F. Bunshah, *Thin Solid Films* **83**, 267 (1981).
- ³³ D. Das and R. Banerjee, *Thin Solid Films* **147**, 321 (1987).
- ³⁴ S. Muranaka, Y. Bando, and T. Takada, *Thin Solid Films* **86**, 11 (1981).
- ³⁵ M. Mizuhashi, *J. Non-Cryst. Solids* **38&39**, 329 (1980).
- ³⁶ E. Gerlach and P. Grosse, *Festkörperprobleme XVII*, 157 (1977).
- ³⁷ T. S. Eriksson and C. G. Granqvist, *J. Appl. Phys.* **60**, 2081 (1986).
- ³⁸ Z. M. Jarzebski and J. P. Marton, *J. Electrochem. Soc.* **123**, 199C (1976); *ibid.* 299C; *ibid.* 333C.
- ³⁹ C. A. Vincent, *J. Electrochem. Soc.* **119**, 515 (1972).
- ⁴⁰ B. Stjerna and C. G. Granqvist, *Appl. Opt.* **29**, 447 (1990).
- ⁴¹ G. Wysecki and W. S. Stiles, *Color Science*, 2nd ed. (Wiley, New York, 1982), p. 256.
- ⁴² B. Stjerna, C. G. Granqvist, A. Seidel, and L. Häggström, *J. Appl. Phys.* **68**, 6241 (1990).
- ⁴³ Y. Nakanishi, Y. Suzuki, T. Nakamura, Y. Hatanaka, Y. Fukuda, A. Fujisawa, and G. Shimaoka, *Appl. Surf. Sci.* **48/49**, 55 (1991).
- ⁴⁴ C. G. Fonstad and R. H. Rediker, *J. Appl. Phys.* **42**, 2911 (1971).
- ⁴⁵ Landolt-Börnstein, *Numerical Data and Functional Relationships in Science and Technology*, New Series III/17f (Springer, Berlin, Heidelberg, 1975).
- ⁴⁶ G. L. Harding, *Sol. Energy Mater.* **12**, 169 (1985).
- ⁴⁷ G. L. Harding, *Thin Solid Films* **138**, 279 (1986).
- ⁴⁸ S.-Y. Zheng, A. M. Andersson, B. Stjerna, and C. G. Granqvist, *Appl. Opt.* **32**, 6303 (1993).
- ⁴⁹ Z. Q. Yin, B. Stjerna, and C. G. Granqvist, *Proc. Soc. Photo-Opt. Instrum. Eng.* **1536**, 149 (1991).
- ⁵⁰ E. Shanti, A. Banerjee, V. Dutta, and K. L. Chopra, *J. Appl. Phys.* **53**, 1615 (1982).
- ⁵¹ V. Casey and M. I. Stephenson, *J. Phys. D* **23**, 1212 (1990).
- ⁵² R. S. Katiyar, P. Dawson, M. Hargreave, and G. R. Wilkinson, *J. Phys. C* **4**, 2421 (1971).
- ⁵³ Z. C. Orel, B. Orel, and M. K. Gunde, *Sol. Energy Mater.* **26**, 105 (1992).
- ⁵⁴ P. A. Cox, R. G. Egdell, J. P. Kemp, F. H. Potter, and C. S. Rastomjee, *J. Electron Spectrosc. Relat. Phenom.* **54/55**, 1173 (1990).
- ⁵⁵ J. C. Manificier, J. Gasiot, and J. P. Fillard, *J. Phys. E* **9**, 1002 (1976).
- ⁵⁶ R. Swanepoel, *J. Phys. E* **16**, 1214 (1983).
- ⁵⁷ D. P. Arndt, R. M. A. Azzam, J. M. Bennett, J. P. Bogogno, C. K. Carniglia, W. E. Case, J. A. Dobrowolski, U. J. Gibson, T. T. Hart, F. C. Ho, V. A. Hodgkin, W. P. Klapp, H. A. Macleod, E. Pelletier, M. K. Purvis, D. M. Quinn, D. H. Stome, R. Swenson, P. A. Temple, and T. F. Thonn, *Appl. Opt.* **23**, 3571 (1983).
- ⁵⁸ B. Bovard, F. J. Van Milligen, M. J. Messerly, S. G. Saxe, and H. A. Macleod, *Appl. Opt.* **24**, 1803 (1985).
- ⁵⁹ E. Shanti, V. Dutta, A. Banerjee, and K. L. Chopra, *J. Appl. Phys.* **51**, 6243 (1980).
- ⁶⁰ J. C. Manificier, M. De Murcia, J. P. Fillard, and E. Vicario, *Thin Solid Films* **41**, 127 (1977).
- ⁶¹ F. Wooten, *Optical Properties of Solids* (Academic, New York, 1981).
- ⁶² R. A. Smith, *Semiconductors* (Cambridge University Press, Cambridge, 1978).
- ⁶³ M. Nagasawa and S. Shionoya, *Solid State Commun.* **7**, 1731 (1969).
- ⁶⁴ E. Shanti, A. Banerjee, and K. L. Chopra, *Thin Solid Films* **88**, 93 (1982).
- ⁶⁵ I. Hamberg, C. G. Granqvist, K.-F. Berggren, B. E. Sernelius, and L. Engström, *Phys. Rev. B* **30**, 3240 (1984).
- ⁶⁶ T. Yamazaki, U. Mizutani, and Y. Iwani, *Jpn. J. Appl. Phys.* **21**, 440 (1982).
- ⁶⁷ T. Tabuchi, K. Yamagishi, and Y. Tarui, *Jpn. J. Appl. Phys.* **26**, L186 (1987).
- ⁶⁸ A. Mani, *J. Mater. Sci. Lett.* **9**, 1106 (1990).
- ⁶⁹ V. Vasu and A. Subrahmanyam, *Thin Solid Films* **189**, 217 (1990).
- ⁷⁰ M. Fantini and I. Torriani, *Thin Solid Films* **138**, 255 (1986).
- ⁷¹ L. I. Popova, M. G. Michailov, V. K. Guerguiev, and A. Shopov, *Thin Solid Films* **186**, 107 (1990).
- ⁷² K. H. Kim and C. G. Park, *J. Electrochem. Soc.* **138**, 2408 (1991).
- ⁷³ J. Bruneaux, H. Cachet, M. Froment, M. Levart, and J. Vedel, *J. Microsc. Spectrosc. Electron.* **14**, 1 (1989).
- ⁷⁴ J. Melsheimer and B. Tesche, *Thin Solid Films* **138**, 71 (1986).
- ⁷⁵ D. Chattopadhyay and H.-J. Queisser, *Rev. Mod. Phys.* **53**, 745 (1981).
- ⁷⁶ M. G. Calkin and P. J. Nicholson, *Rev. Mod. Phys.* **39**, 361 (1967).
- ⁷⁷ J. Lindhard, K. Dan. Vidensk. Selsk. Mat. Fys. Medd. **28**, 1 (1954).
- ⁷⁸ B. E. Sernelius and M. Morling, *Thin Solid Films* **177**, 69 (1989).
- ⁷⁹ B. E. Sernelius, *Phys. Rev. B* **36**, 1080 (1989).
- ⁸⁰ B. E. Sernelius, K. F. Berggren, Z. C. Jin, I. Hamberg, and C. G. Granqvist, *Phys. Rev. B* **37**, 10 244 (1988).
- ⁸¹ M. Born and E. Wolf, *Principles of Optics*, 6th ed. (Pergamon, New York, 1983).
- ⁸² Information from Corning Glass Works, Corning, NY, USA.
- ⁸³ B. Stjerna and C. G. Granqvist, *Proc. Soc. Photo-Opt. Instrum. Eng.* **1272**, 12 (1990).
- ⁸⁴ H. Haitjema, J. J. P. Elich, and C. J. Hoogendoorn, *Sol. Energy Mater.* **18**, 283 (1989).
- ⁸⁵ S. Collins, T. Kachnowski, N. Benczer-Koller, and M. Pasternak, *Phys. Rev. B* **19**, 1369 (1979).
- ⁸⁶ R. Summit, *J. Appl. Phys.* **39**, 3762 (1968).
- ⁸⁷ R. L. Petritz, *Phys. Rev.* **104**, 1508 (1956).